HYDROGEN AND MUONIUM BEHAVIOUR IN DIAMOND

by

SITHOLE MAKGAMATHE JOSEPH

Dissertation submitted in part fulfillment of the requirements

for the degree of

MASTER OF SCIENCE

in the subject

PHYSICS

at the

UNIVERSITY OF SOUTH AFRICA

SUPERVISOR : DR I Z MACHI

CO-SUPERVISOR : DR S H CONNELL (WITS)

MARCH 2005

ABSTRACT

This work is aimed at the understanding of the dynamical behavior of hydrogen in diamond. The investigation was carried out using Transverse Field muon Spin Rotation (TF-μSR) and the Longitudinal Field muon Spin Relaxation (LF-μSR) techniques. The chemical analogy between hydrogen (p^+e^-) and muonium (μ^+e^-) enabled the study of the indirect dynamical behavior of hydrogen in diamond.

The TF-μSR and LF-μSR measurements were carried out in an isotopically pure ^{13}C diamond in the temperature ranges 11 mK - 320 K and 10 K - 400 K, respectively. In the TF-μSR results, the Prompt Absolute Fraction (PAF) of both diamagnetic (μ_{D}^+) and the paramagnetic ($\mathrm{Mu_T}$) states are temperature independent. The spin relaxation rate ($\lambda_{\mu_{\mathrm{D}}^+}$) for the μ_{D}^+ state is non-zero and temperature independent, while that ($\lambda_{\mathrm{Mu_T}}$) of the $\mathrm{Mu_T}$ state is non-zero and temperature dependent. The behavior of $\lambda_{\mu_{\mathrm{D}}^+}$ indicates that the μ_{D}^+ is immobile, while that of $\mathrm{Mu_T}$ indicates the mobility in diamond. The LF-μSR results provide hop rate and associated nuclear hyperfine interaction parameters of the $\mathrm{Mu_T}$ state in diamond.

Keywords: Diamond; Muonium; Hydrogen; Diffusion; μSR; Relaxation rate; Prompt Fraction; Hop rate; Power law dependence

I (**Makgamathe Joseph Sithole**) declare that this is my work. It is being submitted in part fulfillment of the requirement for the degree of Master of Science at the University of South Africa (Pretoria). It has not been submitted before any degree or examination, at any other university.

Signature: ..... Date: .....

Dedication

To my parents

ACKNOWLEDGMENTS

First of all I thank God for giving me the strength of focusing on my studies during hard times. Many thanks to my supervisor **Dr I Z Machi** and co-supervisor **Dr S H Connell** for exposing me to this interesting field. Furthermore, thanks again for giving me the opportunity to be part of the group to conduct the experiments internationally and locally. I would not forget the support you gave during the stressful times for the preparation of my presentation held at the University of Stellenbosch and at the University of the Free State. Thanks to **Mr D Gxawu** with whom I jointly made an experiment, for assisting me with the data analysis.

The experimental part of the research work presented in this dissertation was conducted internationally, at Paul Scherrer Institute (PSI) in Switzerland in Europe and ISIS Facility located at Rutherford Appleton Laboratory (ISIS-RAL) under the supervision of **Dr I Z Machi** (University of South Africa), co-supervision of **Dr S H Connell** (University of Witwatersrand), **Prof. K Bharuth-Ram** (University of KwaZulu-Natal) and **S F J Cox** (ISIS Facility, Rutherford Appleton Laboratory). I was fortunate to have worked under the supervision of these internationally recognized physicists. Their consistent and patient guidance, throughout my MSc studies, is fully appreciated.

I am grateful to **Dr I Z Machi, Mr M L Lekala** and **Dr I Basson** for the academic, social support and encouragement during post-graduate levels of my studies. Many thanks also go to co-workers **Herman, Dr E B Lombardi, Mr G J Rampho, Dr A E Botha** and **Prof. M Braun** for the support I received in connection

with Latex. I would not forget co-students **Mr M Dalton** and **others** during the running of the μSR experiments.

Many thanks to **Mrs R T M Moeketsi**, the administrative officer at the science library, for assisting me with accessing the materials that I needed for my dissertation.

I greatly acknowledge the financial support I received from the **National Research Foundation (NRF)**. I also thank **De Beers Industrial Diamonds Division (Pty) Ltd** for supplying with diamonds during the experiments.

Most of all I thank my father (**Bishop B S Sithole**), mother (**Leah**) and elder brother (**Daniel**) for their support and encouragement throughout my studies. My thanks are also directed to my closest friends **Anikie, Solly, John, Harry, Lucas and Gilbert** and my children **Otsile, Ipeleng** and **Oratilwe** for the encouragement during hard times.

Contents

List of Figures

List of Tables

Chapter 1

Introduction

This work is aimed at studying the behavior of hydrogen in diamond. The understanding of hydrogen behavior in diamond is one of both fundamental and technological interest. However, it is extremely difficult to obtain direct information on isolated hydrogen in diamond using conventional methods, mainly due to its high mobility and reactivity. The chemical analogy between hydrogen (p^+e^-) and muonium (μ^+e^-) enables hydrogen to be studied through muonium. This can be readily achieved by using the muon Spin Rotation or Relaxation (μSR) method. It is, however, recognized that muonium and hydrogen are incorporated in two different ways in samples. Hydrogen is introduced during the time of sample preparation or post-processing and reaches thermal and chemical equilibrium before measurements begin, while muonium is observed within 2.2 μs after implantation of almost 100% spin polarized muons. This means the hydrogen and the muonium are observed in very different time windows after their introduction. The other factor is that in the

case of μSR only one muon at a time (even at the highest intensities of available muon beams) may be present in the diamond, while concentrations as high as 10000 ppm of hydrogen could be incorporated in diamond prior to the conventional measurements. It therefore turns out that muonium mostly occurs as an isolated centre in diamond which makes it possible to explore its dynamical behaviour. The latter provides shorter term dynamics in diamonds, where hydrogen is expected to have interacted with any defects or impurities by the time conventional measurements are conducted.

The above discussion shows that the defected nature of even the purest diamonds available contain hydrogen in a complex form, while the short time window of μSR provides a unique opportunity of indirectly exploring hydrogen diffusion during its early presence in the sample. Obvious caveats apply due to the lighter mass of muonium in comparing dynamical information which is inferred from the depolarization rate of the muon ensemble. Further fundamental information on diamond and its defects is provided below.

1.1 Diamond

Diamond is the hardest natural substance and the word is derived from Greek *Adamas*, meaning 'hardest steel'. A diamond is an allotrope of carbon and, no matter what its size, each diamond can be considered to be a single molecule of carbon. The element, carbon, has four valence electrons that are spread in the s and p orbitals. In order to create covalent bonds in the diamond, the s orbital

mixes with the three p orbitals to form sp^3 hybridization. The four valence electrons are thus equally distributed among the sp^3 orbitals, while each orbital points to one of the four corners of a tetrahedron. Strong covalent bonds form maintaining this geometry. The tetrahedral structure, together with the highly directed charge density, give strength and stability to the bonds. Consequently, all the bonds in diamond are of the same length (1.545 Å), with the same bond angle (109.47°). Diamond has an isomeric crystallography. The arrangement is based on the face centered cubic or FCC lattice with the basis 000, $\frac{1}{4}\frac{1}{4}\frac{1}{4}$. Thus, to each of the four atoms making up the FCC cell an extra atom is added to give eight atoms per cubic cell. Each unit cell of a diamond has a lattice constant of 0.357 nm and hence the volume of 4.54×10^{-23} cm^3/unit cell. Since there are 8 atoms per unit cell, the atomic density is found to be 1.763×10^{23} atoms/cm^3, and this leads to the density of about 3.52 g/cm^3 for diamond. As shown in Figure 1.1, atoms have the tetrahedral co-ordination characteristic of the covalent bonding of the sp^3 hybrid orbitals.

The maximum packing fraction for diamond may be calculated using the expression:

$$f = \frac{nV_a}{V_c},$$

where V_a is the volume of a spherical atom (i.e. $V_a = \frac{4}{3}\pi r^3$), V_c the volume of a cube (i.e $V_c = a^3$) and n is the number of atom per unit cell. In diamond cube (dc), substitution of $n = 8$, the nearest neighbor distance ($2r = a\sqrt{3}/4$) and hence the atomic radius $a\sqrt{3}/8$, lead to the maximum packing fraction

$$\begin{aligned} f &= \pi\sqrt{3}/16 \\ &= 0.34 \end{aligned} \tag{1.1}$$

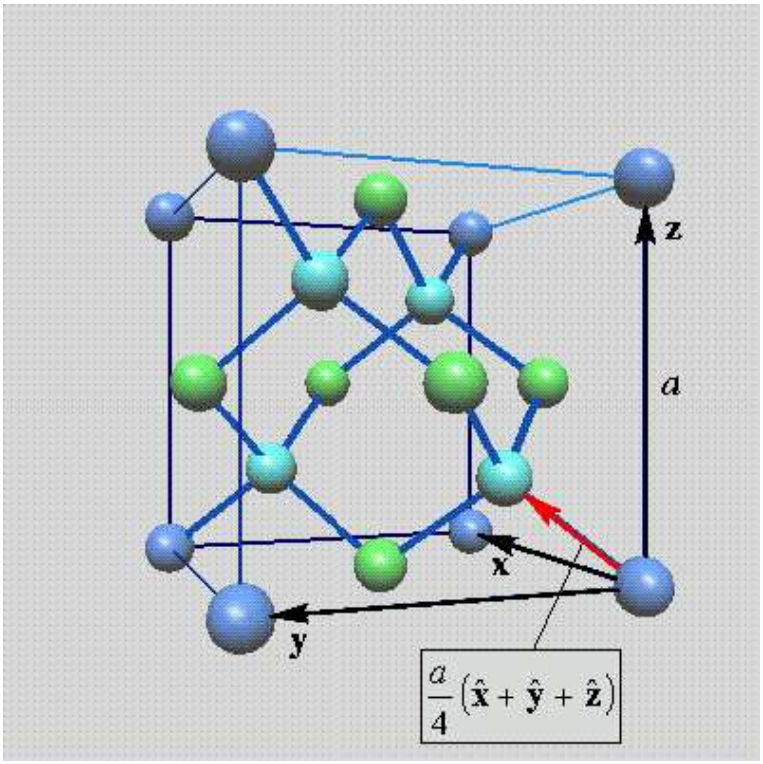

Figure 1.1: Conventional cubic cell of the diamond lattice.

Comparison of this value to BCC ($f = 0.680$) and FCC ($f = 0.740$) shows that the diamond is much more open.

Diamond has received increasing attention recently because of its very attractive physical and electronic properties, and the real possibility of being able to engineer new diamond-based materials and devices. Many of the physical, chemical, optical and electronic properties of diamond represent (near) extremes when compared to other materials [1]. Diamond has unique properties such as high electrical resistivity ($10^{13} - 10^{16}$ Ohm-cm), high thermal conductivity (20.0 W/cm-K), low thermal expansion coefficient (1.1 ppm K^{-1}), high thermal diffusivity (10 cm^2 s^{-1}), wide forbidden energy band gap (5.45 eV), high density (3.52 g/cm^3), etc [2] and hence is regarded as a good material to study (for technological and academic interests). Due to these unique properties, diamond is expected to have great potential research and commercial applications that are now becoming a reality, due to recent developments in the synthesis of diamond. It is now possible to produce synthetic diamonds using the Chemical Vapor Deposition (CVD) technique. The availability of large CVD diamond plates, showing similar thermal properties to natural (type IIa) single crystal diamond, has opened a host of new possible applications in which diamond can be used, for example, in the heat management of electronic and optoelectronic devices. This technique is known as a CVD process, where single-crystal and polycrystalline films of diamond can be produced by the deposition of carbon from hydrocarbon gases onto various substrates such as diamond, tungsten and silicon. In addition, single-crystal diamonds are now synthesized from graphite or from small crystals of diamond in the presence of solvent/ catalyst metals such as iron, cobalt and nickel. High temperature and enormous pressures are needed for this

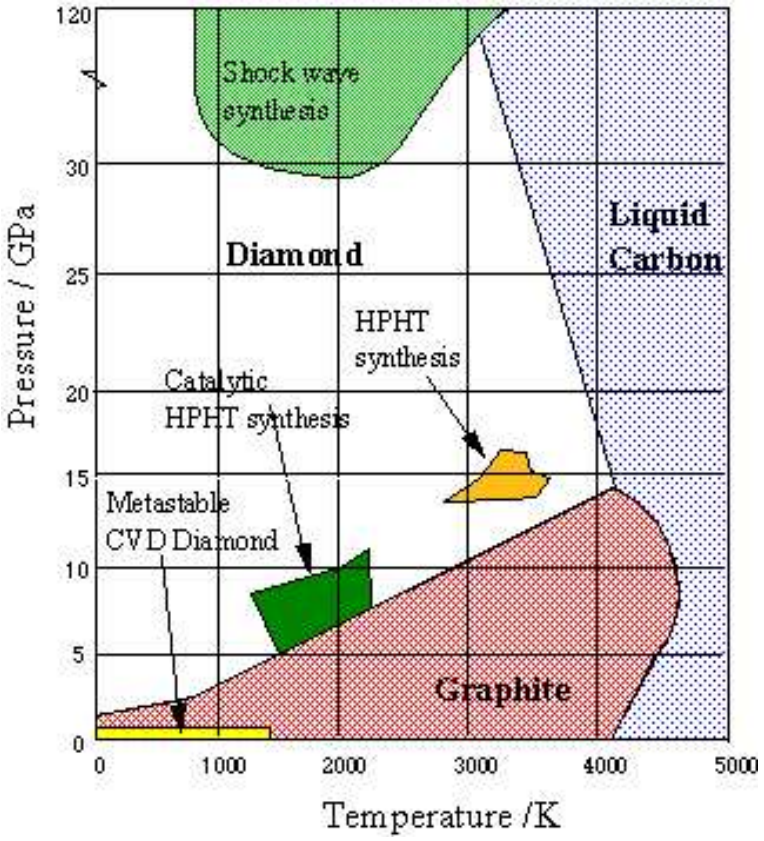

Figure 1.2: Phase diagram for Carbon [28].

process, typical temperatures and pressures are in the ranges 1550-1600°C and 5-6 GPa, respectively, (see Figure 1.2 for catalytic HPHT synthesis). These conditions are similar to those that exist 100 miles below the earth's surface, where diamond crystals are formed. These developments have stimulated academic interest in the solid state physics community. One of the intriguing topics in solid state physics is the effect of impurities on the structural and dynamical properties of an ideal crystal. The overwhelming majority of both natural and synthetic diamonds contains an appreciable amount of nitrogen impurity which is a determining factor of the quality of diamond.

Scientists in the 1930s devised a simple scheme to categorize diamonds into two main groups, or types, i.e type I and type II. Historically, these two categories have been distinguished by differences among diamonds in their ultraviolet transparency, and in their infrared spectra. Diamonds are classified into different types, depending on the nature and concentration of defects (mostly nitrogen) present in the bulk. Physically, there are four well-known types of diamond and these are distinguished through the relative concentration of nitrogen and boron impurities.

- The type I diamonds are the most abundant category in nature. Features in the visible and infrared spectra of type I diamonds have been attributed to the presence of nitrogen atoms in various configurations and contain between 150 and 5000 ppm of nitrogen. These diamonds are sub-divided into types Ia and Ib, depending on the form that the nitrogen atoms take in a particular diamond.
  - Type Ia diamonds contain aggregate nitrogen defects known as A-centres

(two nearest neighbor substitutional nitrogen atoms, N-N) and B-centres (four substitutional nitrogen atoms surrounding a vacancy, $N_2 - \text{vacancy} - N_2$) (see Figure 1.3).

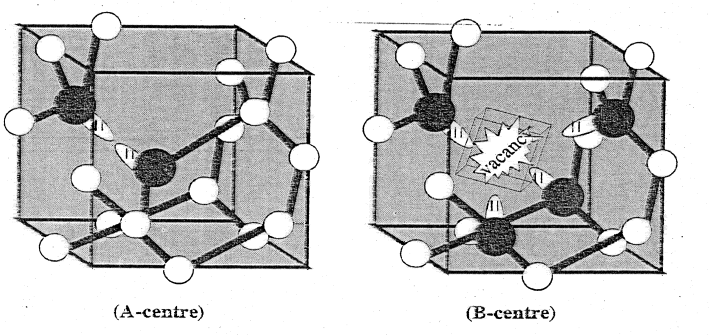

Figure 1.3: Illustration of A- and B-centres in diamond. The heavily shaded atoms are nitrogen, each with a lone electron pair. The unshaded atoms are Carbon [29].

  - Type Ib diamond is characterized by paramagnetic isolated single substitutional nitrogen.

- The type II diamond contains between 14 and 40 ppm [16] of nitrogen, and are subdivided into IIa and IIb. The former is known to be relatively pure in nature (with a relatively large mosaic spread, $\geq 0.1^0$) and the latter is a semiconductor with an active dopant/boron.

Other defects could include naturally and deliberately introduced impurities such as phosphorus, iron, arsenic, boron, oxygen and lithium. There are also ion-induced vacancies such as neutral (V^0), negatively charged vacancies (V^-) and positively charged vacancies (V^+) [3,4,5]. Among all defects present in the diamond, hydrogen is found to be of significant interest, due to its capability to passivate active dopants,

its role in the synthesis of CVD diamond, its role in determining surface properties, its (potential) role in the shallowing of deep level electronic states by aggregation with other defects, its (potential) role in stabilizing extended intrinsic defects and the fact that it is conceptually simple to treat theoretically.

1.2 Hydrogen in diamond

The interest in the study of hydrogen in diamond has arisen mostly from the quest to understand its influence on the electrical properties of diamond, in view of the potential of diamond to play a significant role in semiconductor devices. As in many other materials, light volatiles such as hydrogen could play a significant role in diamond as much as it could also contribute to some setbacks in the advancement of diamond technology. Hydrogen (H) is known to passivates active dopants [8] and its hydrogen chemistry dominates CVD growth mechanism [9,10] and subsequent diamond layer properties [11], making it difficult to eliminate the incorporation of hydrogen during the growth process. Recent experiments show evidence that H is a strong candidate to form hydrogenated molecular complexes which lead to a shallowing of donor levels e.g BH_2 and NHN. Furthermore, the donor level of the hydrogenated defect is shallower than the isolated impurity [50].

Already there are negative factors associated with the presence of hydrogen in diamond. One of the negative factors include the influence of hydrogen on the electrical and optical properties of diamond [12]. In addition, from the effects of, for example, the formation of an electrically conducting surface by hydrogen, it was reported that

an increase in hydrogen concentration could result in an increase of the electrical conductivity in diamond [13]. Since boron, a shallow acceptor, can be passivated by hydrogen, it is possible that some of the difficulties associated with the production of electrically active donors could be attributed to the presence of hydrogen mostly incorporated during the growth of diamond. The above factors indicate that there are still many unknowns about hydrogen behavior in diamond. As an example, the shallowing of defect level by hydrogenated molecular complexes e.g BH_2, the positions, the diffusivity and the nature of multi-hydrogen trapping at impurities are not yet clear. Most of the lack on the understanding of hydrogen behavior in diamond has been due to the difficulty in conventional studies of hydrogen, due to hydrogen forming diamagnetic complexes. It is extremely difficult to detect hydrogen using conventional spectroscopic methods because of its high diffusivity and reactivity with other defects coupled to the relatively impure nature of even the best available diamond. The detailed chemistry of its catalytic role in diamond synthesis is envisaged to proceed via a range of intermediate bonded interactions and complexes. It is increasingly important to distinguish between the influence of bulk and grain-boundary phenomena. It has been found that interstitial hydrogen binds strongly to impurities in diamond [17], therefore it is possible that multiple trapping of hydrogen at dopants will occur.

From a theoretical perspective, a number of different configurations have been proposed for hydrogen trapping in the bulk of diamond [54]; trapping at vacancies, dislocations, or at defects such as A and B centres [18,19] and the auto-trapped systems like the bond centered (H_{BC}), the bonding-anti-bonding (H_2^*) and the tetrahedral molecular (H_{2T}) configurations [20-22]. For an example neutral hydrogen was found

to be more stable (2.4 eV) within an A-centre than in the bond-centered site [23]. From the experimental point of view, the muon spin rotation (μSR) has, to date, offered invaluable information on the study of hydrogen in diamond.

1.3 Muonium

Due to the chemical analogy between muonium (Mu $\equiv \mu^+e^-$) and hydrogen (H $\equiv p^+e^-$) (see Table 1.1 and 1.2, respectively), muon Spin Rotation (μSR) experiments are frequently used in the study of hydrogen in solid-state materials, as it is extremely difficult to study intrinsic hydrogen using conventional methods; mainly due to the high reactivity of hydrogen with defects. μSR measurements in diamond have been extensively conducted in the past where configurations of different muonium states such as the tetrahedral interstitial ($\mathrm{Mu_T}$), the bond-centered paramagnetic ($\mathrm{Mu_{BC}}$), the diamagnetic (μ_D) and muonium at a site of less than axial symmetry (Mu_X) were identified [24,52,53]. See Figure 1.4. The $\mathrm{Mu_{BC}}$ state, with anisotropic hyperfine parameters, is known to be more stable state while the $\mathrm{Mu_T}$ state, with an isotropic hyperfine parameter, forms soon after implantation and is known to diffuse rapidly [25]. In addition, a new muonium state, Mu_X, represents a paramagnetic configuration with less than axial symmetry and is also associated with aggregated nitrogen in the form of A- or B- centres [26]. Relatively little is known about μ_D.

From the fact that positively charged muons μ^+ behave like light unstable protons in condensed matter, thus preferentially occupy interstitial regions in semiconductors

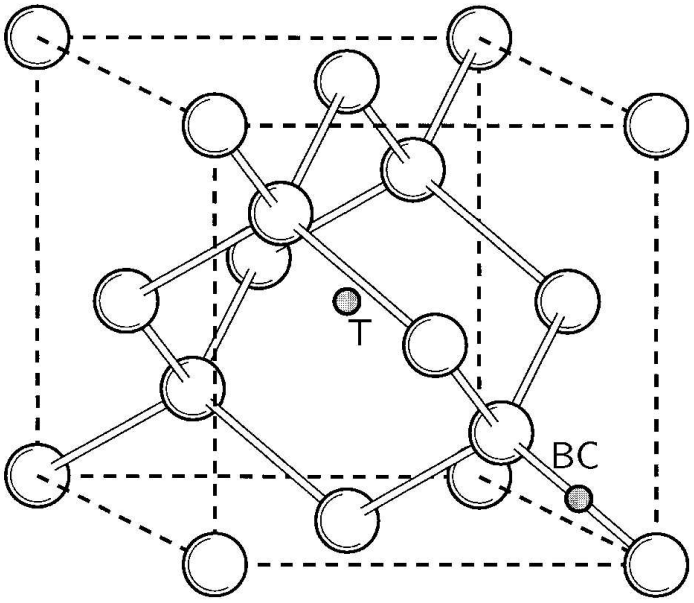

Figure 1.4: The crystal structure of diamond, showing the possible muonium sites (T=tetrahedral sites, BC=bond-centre site).

and insulators resulting in the capture of electrons to form paramagnetic muonium states. Some μSR experiments have contributed in the understanding of the formation of muonium in solid-state materials. For example, the suppression of anomalous muonium signal with electric field suggests that muonium formation proceeds via transport of excess electrons from the ionization track to the muons [28]. Weak electric fields of about 8 kV/cm are sufficient to suppress the muonium formation, suggesting electron capture into excited hydrogenic states. Irrespective of the state of matter, three different regions of energy loss are distinguishable: Firstly, at high velocity regime, $v \sim c/3$, the muon should behave like any fast charged particle and undergo energy loss by excitation and Bethe-Bloch ionization of the medium. This enables the calculation of the slowing down time between the initial and final energy states, to be about 10^{-10}s. In the second region, no significant amount of muonium should form until the kinetic energy drops to several tens of keV, where the muon velocity becomes comparable to the orbital velocity of electrons of the medium. The time required to reach this energy ranges between 0.1 and 10.0 ps. Once the region is reached, the charge exchange collisions become important. This results in the capturing of an electron by the muon from the medium to form muonium. Lastly, at an energy of the order 100 eV, charge exchange is no longer dominant and the fraction of the muonium at these energies is expected to be influenced by the relative electron affinities of the muon and atoms of the sample. In materials with ionization potentials smaller than that of muonium (13.54 eV) most muons are expected to emerge from this stage as hot muonium atoms. 'Hot' muonium formation is a 'prompt' process, occurring during a time when the muon is rapidly losing energy, within a few tens of ps after entering a condensed sample. Muonium formation after the muon has come to thermal equilibrium with its surrounding requires time

for electrons to diffuse to the muon, and is therefore termed 'delayed' muonium formation.

Table 1.1: Comparison of some important properties of the muon (μ^+) and the proton (p^+).

NUCLEI	muon (μ^+)	proton (p^+)
mass (m_e)	206.768	1836.15
Charge (e)	+1	+1
Spin	1/2	1/2
Half-life (μs)	2.2	stable

Table 1.2: Comparison of the properties of the muonium (μ^+e^-) and hydrogen (p^+e^-).

ATOMS	Muonium (Mu)	Hydrogen (H)
Reduced mass (m_e)	0.995	0.999
Radius (Å)	0.531	0.529
Ionization energy (eV)	-13.54	-13.59
H.F. frequency (GHz)	4.46	1.42

1.4 Current research aims

The work is aimed at acquiring the general understanding of the dynamical behavior of hydrogen in diamond materials. This has been made possible by the chemical

analogue between hydrogen and muonium. The current μSR measurements have offered an opportunity to provide better insights into the behavior of the hydrogen-like "atom" after the promptly formed muon(ium) states and the spin relaxation rates were measured in an isotopically pure ^{13}C diamond. The spin-$\frac{1}{2}$ ^{13}C nuclei have non-zero nuclear moments which could cause muons to undergo spin relaxation as a function of their dynamics within the sample.

Chapter 2

Theoretical Aspects

2.1 Muon Spin Rotation (μSR) Spectroscopy in Diamond

In this experiment, 100% spin polarized muons were implanted into the bulk of diamond. In a muonium atom, the magnetic moments of the positive muon and electron interact with one another via the hyperfine interaction, and in turn they both interact with the applied magnetic field via the Zeeman interaction. In addition, muonium in a solid state material may experience a nuclear hyperfine interaction with neighboring host nuclei. In an ideal pure crystal, all these interactions can be non dissipative, hence the resulting muon polarization could consist of a sum of undamped oscillating components. The oscillation frequencies for a particular

set of interactions can be calculated using elementary quantum mechanics, and the comparison with experiment yields the hyperfine and nuclear hyperfine interaction tensors and the electron or muon g-values. The term "muonium spectroscopy" is used in this review to describe the analysis of these non-dissipative interactions. However, muonium in a real solid host experiences interactions that lead to a loss of polarization, i.e a certain fraction of the spin-phase coherence of the muon ensemble is lost (known as a T_2 mechanism) or the fraction of the spin is transferred/shared with the environment (known as a T_1 mechanism). These dissipative effects result in the observation of non-zero relaxation rate of the muon spin ensemble. Various theoretical models which treat these interactions in terms of perturbations of either the Zeeman or the hyperfine interaction, i.e, either as a randomly fluctuating magnetic field or as a persistent or an irreversible change in the hyperfine interaction, are used. The use of these models is aimed at fitting the experimental data, from which parameters of interest are extracted. Comparison of the results of these theories with experiment yields information on the dynamics of muonium and the perturbing effects of its environment. In this review "muonium dynamics" is used to describe such dissipative phenomena. Investigations of these perturbation effects depend on the basic knowledge of the spin Hamiltonians for muonium states, formed in the presence or absence of the external applied magnetic field.

The muonium's electron may show a significant spin probability density at the site of the neighboring host nuclei. If these nuclei have spin, a so-called "Nuclear Hyperfine Interaction" (NHFI), also called super hyperfine interaction, arises. This interaction and the nuclear Zeeman interaction add at least two terms to the unperturbed muonium spin Hamiltonian with a static magnetic field along the z-direction and

this results in the perturbed spin Hamiltonian,

$$\begin{aligned} \mathrm{H(NHFI)} &= h\bar{S}_\mu \cdot \bar{A}_{\mathrm{Mu_T}} \cdot \bar{S}_e - \mathrm{g}_\mu \mu_\mu S_z^\mu B_z - \mathrm{g}_e \mu_\mathrm{B} S_z^e B_z \\ &\quad + h \sum_{n=1}^{N} \bar{S}_n \cdot \bar{A}_n \cdot \bar{S}_e - \sum_{n=1}^{N} \mathrm{g}_n \mu_n S_z^n B_z \end{aligned} \tag{2.1}$$

In the unperturbed terms of Equation 2.1 , the first term is the hyperfine coupling between the muon and electron spins with $\bar{A}_{\mathrm{Mu_T}}$ being the muonium hyperfine (HF) frequency (about $2{\times}10^{10}$ s^{-1} rad for the ground state in vacuum). The second and third terms are Zeeman interactions for the muon and electron spins with the applied magnetic field (B), respectively. The S, g, and μ terms are the spins, g-factors and magnetic moments of the various particles. In the terms regarded as perturbations, the summation are over all nearby nuclei. The nuclear quadrupole interactions are known to be negligibly small [49]. The nuclear hyperfine interaction (NHFI) between the muonium and neighboring nuclear dipoles is characterized by the frequency $\bar{A}_n$. The NHFI term in Equation 2.1 and so may represent either an average magnetic dipole interaction, in the local field approximation, or a contact interaction, in the event that the muonium electron's wave function overlaps with the surrounding nuclei. If muonium and hydrogen occupy equivalent lattice sites, the NHFI frequency for nuclei adjacent to muonium is expected to differ (due to zero point motion) from the value of those adjacent to interstitial hydrogen (protium) itself, which has been measured by ESR to be 15 MHz [54]. It is the details of this interaction that sets the time scale of the spin relaxation rate. Qualitatively, the nuclear hyperfine interaction leads ultimately to relaxation of the muon polarization through mechanisms dependent of the details of the experimental situation.

In the transverse magnetic field scenario, the relaxation rate T_2^{-1} of the muonium

precession signal has a simple form in two limits; namely if muonium "hops" from site to site at a rate $\tau_{\rm c}^{-1}$ which is much larger than the NHFI frequency δ (fast hopping limits), then the transverse relaxation rate is given by $T_2^{-1} \sim \delta^2\tau_{\rm c}$, which is proportional to the effective width of the local-field distribution due to nuclear hyperfine interaction, motionally averaged (hence "narrowed") by fast muonium diffusion with $\tau_{\rm c}^{-1} \gg \delta$. For very slow diffusion ($\tau_{\rm c}^{-1} \leq \delta$), muon spin relaxation takes place on a time scale shorter than the muon average lifetime, τ, and $T_2^{-1} \sim \delta$. For this reason, the parameter δ is sometimes referred to as the "static width" due to NHFI. From above, it transpires that in this regime, $\tau_{\rm c} > \tau$ or the muon stays at the site long compared to its life time. This means that each muon in the ensemble is at a site which has a different net field as the local field due to the ^{13}C nuclei is random. The theory that explain interaction between muonium and ^{13}C nuclei is explained below.

The eigenvalues for Equation 2.1 are obtained by solving the spin Hamiltonian (see Equation 2.1) that can be written as,

$$\mathrm{H(NHFI)} \;=\; \frac{\hbar\omega_0}{4}\bar{\sigma}\cdot\bar{\mathrm{S}} - \frac{\hbar}{2}\omega_\mu\sigma_z + \frac{\hbar}{2}\omega_e\mathrm{S}_z + \frac{\hbar\Omega}{4}\bar{\mathrm{S}}\cdot\bar{\tau} - \frac{\hbar\omega_n}{2}\tau_z \qquad (2.2)$$

where,

$\omega_0 = 2\pi\bar{\mathrm{A}}_{\mathrm{Mu_T}}$, $\omega_e = \mathrm{g}_e\mu_{\mathrm{B}}B/\hbar$,

$\omega_i = \mathrm{g}_i\mu_i B/\hbar$, where $i = \mu, n$

$\bar{\sigma} = 2\bar{S}_\mu$, $\bar{\mathrm{S}} = 2\bar{S}_e$, $\Omega = 2\pi\mathrm{A}_n$, and $\bar{\tau} = 2\bar{S}_n$, where $\bar{\tau}$ is the Pauli spin operator for the nucleus. This Hamiltonian is based on the assumption that the NHFI term is isotropic because only the $\mathrm{Mu_T}$ state is observed in the sample.

In the current work, twenty spin states written as $\mid m^\mu m^e m^n\rangle$ can be chosen from

the interaction of Mu via isotropic NHFI. Taking into account that each Mu_T is surrounded by four ^{13}C atoms, the spin basis have the following spin permutation: $|+,+,+4>$; $|+,+,+2>$; $|+,+,0>$; $|+,+,-2>$; $|+,+,-4>$; $|+,-,+4>$; $|+,-,+2>$; $|+,-,0>$; $|+,-,-2>$; $|+,-,-4>$; $|-,+,+4>$; $|-,+,+2>$; $|-,+,0>$; $|-,+,-2>$; $|-,+,-4>$; $|-,-,+4>$; $|-,-,+2>$; $|-,-,0>$; $|-,-,-2>$; and $|-,-,-4>$.

Now from Equation 2.3, the spin Hamiltonian can be rewritten in terms of operators for electron, muon and nuclear spins as follows;

$$\begin{aligned} \mathrm{H} &= \frac{\hbar\omega_0}{4}\bar{\sigma}^{\mu}\cdot\bar{\sigma}^{e} - \frac{\hbar}{2}\omega_{\mu}\sigma_z^{\mu} + \frac{\hbar}{2}\omega_z^{e}\sigma_z^{e} + \frac{\hbar}{4}\Omega^{n}\bar{\sigma}^{e}\cdot\bar{\sigma}^{n} - \frac{\hbar}{2}\omega_n\sigma_z^{n} \\ &= \frac{\hbar\omega_0}{4}(\sigma_x^{\mu}\sigma_x^{e} + \sigma_y^{\mu}\sigma_y^{e} + \sigma_z^{\mu}\sigma_z^{e}) + \frac{\hbar}{4}\Omega(\sigma_x^{n}\sigma_x^{e} + \sigma_y^{n}\sigma_y^{e} + \sigma_z^{n}\sigma_z^{e}) \\ &\quad + \frac{\hbar}{2}\omega_e\sigma_z^{e} - \frac{\hbar}{2}\omega_{\mu}\sigma_z^{\mu} - \frac{\hbar}{2}\sigma_n\sigma_z^{n}. \end{aligned} \tag{2.3}$$

Now letting

$\alpha = \hbar\omega_0/4$,

$\beta = \hbar\Omega/4$, and

$\gamma^e = \hbar\omega_e/2$, $\gamma^{\mu} = \hbar\omega_{\mu}/2$ and $\gamma^n = \hbar\omega_n/2$,

results in the spin Hamiltonian of the form,

$$\begin{aligned} \mathrm{H} &= \alpha(\sigma_x^{\mu}\sigma_x^{e} + \sigma_y^{\mu}\sigma_y^{e} + \sigma_z^{\mu}\sigma_z^{e}) + \beta(\sigma_x^{n}\sigma_x^{e} + \sigma_y^{n}\sigma_y^{e} + \sigma_z^{n}\sigma_z^{e}) \\ &\quad + \gamma^{e}\sigma_z^{e} - \gamma^{\mu}\sigma_z^{\mu} - \gamma^{n}\sigma_n\sigma_z^{n}, \end{aligned} \tag{2.4}$$

where σ^e, σ^{μ} and σ^n are operators for electron, muon and nuclear spins respectively. Evaluation of Equation 2.4 results in

$\|1\rangle$	$\|2\rangle$	$\|3\rangle$	$\|4\rangle$	. . .	$\|19\rangle$	$\|20\rangle$
$H_{1,1}$	$H_{1,2}$	$H_{1,3}$	$H_{1,4}$	. . .	$H_{1,19}$	$H_{1,20}$
$H_{2,1}$	$H_{2,2}$	$H_{2,3}$	$H_{2,4}$	. . .	.	.
.	.	.	.	. . .	.	.
.	.	.	.	. . .	.	.
.	.	.	.	. . .	.	.
$H_{20,1}$	$H_{20,2}$	$H_{20,3}$	$H_{20,4}$	. . .	$H_{20,19}$	$H_{20,20}$

with diagonal elements given by

$$H_{1,1} = \hbar/4(\omega_0 + 4\Omega) + \hbar/2(\omega_e - \omega_\mu - 4\omega_n)$$
$$H_{2,2} = \hbar/4(\omega_0 + 2\Omega) + \hbar/2(\omega_e - \omega_\mu - 2\omega_n)$$
$$H_{3,3} = \hbar\omega_0/4 + \hbar/2(\omega_e - \omega_\mu)$$
$$H_{4,4} = \hbar/4(\omega_0 - 2\Omega) + \hbar/2(\omega_e - \omega_\mu + 2\omega_n)$$
$$H_{5,5} = \hbar/4(\omega_0 - 4\Omega) + \hbar/2(\omega_e - \omega_\mu + 4\omega_n)$$
$$H_{6,6} = -\hbar/4(\omega_0 - 4\Omega) + \hbar/2(\omega_e + \omega_\mu - 4\omega_n)$$
$$H_{7,7} = -\hbar/4(\omega_0 - 2\Omega) + \hbar/2(\omega_e + \omega_\mu - 2\omega_n)$$
$$H_{8,8} = -\hbar\omega_0/4 + \hbar/2(\omega_e + \omega_\mu)$$
$$H_{9,9} = -\hbar/4(\omega_0 + 2\Omega) + \hbar/2(\omega_e + \omega_\mu + 2\omega_n)$$
$$H_{10,10} = -\hbar/4(\omega_0 + 4\Omega) + \hbar/2(\omega_e + \omega_\mu + 4\omega_n)$$
$$H_{11,11} = -\hbar/4(\omega_0 + 4\Omega) - \hbar/2(\omega_e + \omega_\mu + 4\omega_n)$$
$$H_{12,12} = -\hbar/4(\omega_0 + 2\Omega) - \hbar/2(\omega_e + \omega_\mu + 2\omega_n)$$
$$H_{13,13} = -\hbar\omega_0/4 - \hbar/2(\omega_e + \omega_\mu)$$
$$H_{14,14} = -\hbar/4(\omega_0 - 2\Omega) - \hbar/2(\omega_e + \omega_\mu - 2\omega_n)$$

$H_{15,15} = -\hbar/4(\omega_0 - 4\Omega) - \hbar/2(\omega_e + \omega_\mu - 4\omega_n)$

$H_{16,16} = \hbar/4(\omega_0 - 4\Omega) - \hbar/2(\omega_e - \omega_\mu + 4\omega_n)$

$H_{17,17} = \hbar/4(\omega_0 - 2\Omega) - \hbar/2(\omega_e - \omega_\mu + 2\omega_n)$

$H_{18,18} = \hbar\omega_0/4 - \hbar/2(\omega_e - \omega_\mu)$

$H_{19,19} = \hbar/4(\omega_0 + 2\Omega) - \hbar/2(\omega_e - \omega_\mu - 2\omega_n)$

$H_{20,20} = \hbar/4(\omega_0 + 4\Omega) - \hbar/2(\omega_e - \omega_\mu - 4\omega_n)$

The non-zero off diagonal elements are as follows

$H_{4,11} = H_{11,4} = H_{5,12} = H_{12,5} = H_{9,16} = H_{16,9} = H_{10,17} = H_{17,10} = \hbar\sqrt{2}\Omega$

$H_{6,11} = H_{11,6} = H_{7,12} = H_{12,7} = H_{8,13} = H_{13,8} = H_{9,14} = H_{14,9} = H_{10,15} = H_{15,10} = \hbar\omega_0/2$

The rest of the elements are zero.

Now diagonalize and the corresponding unperturbed or 0^{th}-order energies for $A_n = 0$ are

$E_1 = H_{3,3}/\hbar = \omega_0/4 + 1/2(\omega_e - \omega_\mu) = \omega_0/4 + \omega_-$

$E_2 = H_{8,8}/\hbar = -\omega_0/4 + 1/2(\omega_e + \omega_\mu) = -\omega_0/4 + \omega_+$

$E_3 = H_{18,18}/\hbar = \omega_0/4 - 1/2(\omega_e - \omega_\mu) = -\omega_0/4 - \omega_-$

$E_4 = H_{13,13}/\hbar = -\omega_0/4 - 1/2(\omega_e + \omega_\mu) = -\omega_0/4 - \omega_+$

and for $A_n \neq 0$, the energies are as follows

$E_1 = H_{3,3}/\hbar = \omega_0/4 + \omega_-$

$E_{1^+} = H_{1,1}/\hbar = \omega_0/4 + \omega_- + 1/4(\Omega - 2\omega_n)$

$E'_{1^+} = H_{2,2}/\hbar = \omega_0/4 + \omega_- + 1/2(\Omega/2 - \omega_n)$

$$E_{1^-} = H_{4,4}/\hbar = \omega_0/4 + \omega_- - 1/2(\Omega/2 - \omega_n)$$
$$E'_{1^-} = H_{5,5}/\hbar = \omega_0/4 + \omega_- - 1/4(\Omega - 2\omega_n)$$

$$E_2 = H_{8,8}/\hbar = -\omega_0/4 + \omega_+$$
$$E_{2^+} = H_{6,6}/\hbar = -\omega_0/4 + \omega_+ + 1/4(\Omega - 2\omega_n)$$
$$E'_{2^+} = H_{7,7}/\hbar = -\omega_0/4 + \omega_+ + 1/2(\Omega/2 - \omega_n)$$
$$E_{2^-} = H_{9,9}/\hbar = -\omega_0/4 + \omega_+ - 1/2(\Omega/2 - \omega_n)$$
$$E'_{2^-} = H_{10,10}/\hbar = -\omega_0/4 + \omega_+ - 1/4(\Omega - 2\omega_n)$$

$$E_3 = H_{18,18}/\hbar = -\omega_0/4 - \omega_-$$
$$E_{3^-} = H_{16,16}/\hbar = -\omega_0/4 - \omega_- - 1/4(\Omega - 2\omega_n)$$
$$E'_{3^-} = H_{17,17}/\hbar = -\omega_0/4 - \omega_- - 1/2(\Omega - 2\omega_n)$$
$$E_{3^+} = H_{19,19}/\hbar = -\omega_0/4 - \omega_- + 1/2(\Omega/2 - \omega_n)$$
$$E'_{3^+} = H_{20,20}/\hbar = -\omega_0/4 - \omega_- + 1/4(\Omega - 2\omega_n)$$

$$E_4 = H_{13,13}/\hbar = -\omega_0/4 - \omega_+$$
$$E_{4^-} = H_{11,11}/\hbar = -\omega_0/4 - \omega_+ - 1/4(\Omega - 2\omega_n)$$
$$E'_{4^-} = H_{12,12}/\hbar = -\omega_0/4 - \omega_+ - 1/2(\Omega/2 - \omega_n)$$
$$E_{4^+} = H_{14,14}/\hbar = -\omega_0/4 - \omega_+ + 1/2(\Omega/2 - \omega_n)$$
$$E'_{4^+} = H_{15,15}/\hbar = -\omega_0/4 - \omega_+ + 1/4(\Omega - \omega_n)$$

where $\omega_\pm = (\omega_e \pm \omega_\mu)/2$.

In general, the corresponding first-order energies are given by equations

$$\begin{aligned}
\mathrm{E}'_1/\hbar &= \frac{\omega_0}{4} + \omega_- - \sum_{k=1}^{N_G} \omega_k M_k + \frac{1}{2}\sum_{k=1}^{N_G} \Omega_k M_k, \\
\mathrm{E}'_2/\hbar &= -\frac{\omega_0}{4} + \frac{\omega_+}{cos2\varsigma} - \sum \omega_k M_k + \frac{cos2\varsigma}{2}\sum \Omega_k M_k, \\
\mathrm{E}'_3/\hbar &= \frac{\omega_0}{4} - \omega_- - \sum \omega_k M_k - \frac{1}{2}\sum \Omega_k M_k, \\
\mathrm{E}'_4/\hbar &= -\frac{\omega_0}{4} - \frac{\omega_+}{cos2\varsigma} - \sum \omega_k M_k - \frac{cos2\varsigma}{2}\sum \Omega_k M_k. \qquad (2.5)
\end{aligned}$$

The field dependence of these precession frequencies is shown in the Breit-Rabi-diagram of Figure 2.1, Figure 2.2 and Figure 2.3 for $\mathrm{A}_n = 0$, $\mathrm{A}_n = 500$ MHz and $\mathrm{A}_n = 1000$MHz, respectively, where the ratio E_i/A is plotted as a function of the applied magnetic field B.

In Figure 2.1 (for $\mathrm{A}_n = 0$ MHz) the muonium state is free from interaction with nuclear spins, hence no line splitting is expected. In Figure 2.2 and 2.3, for A_n=500 MHz and A_n=1000 MHz, respectively, a muonium state interacts with four neighboring nuclei of spin-1/2, hence the splitting and the multiple avoided level crossings resonances occur. Evident in Figure 2.2 and 2.3 is that increasing the nuclear hyperfine parameter results in enhanced splitting of lines. The above eigenvalues enable the determination of the muon spin precession frequencies from making use of $\omega_{i,j} = 2\pi\nu_{i,j} = (\mathrm{E}_i - \mathrm{E}_j)/\hbar$ for $i \neq j$ and $i, j = 1, 2, 3, 4$, respectively.

Having determined spin precession frequencies (from the energy eigenvalues) and eigenvectors for the muonium state, then the time-dependent spin polarization $P(t)$ of muonium may be obtained as follows. The density matrix formalism is of the

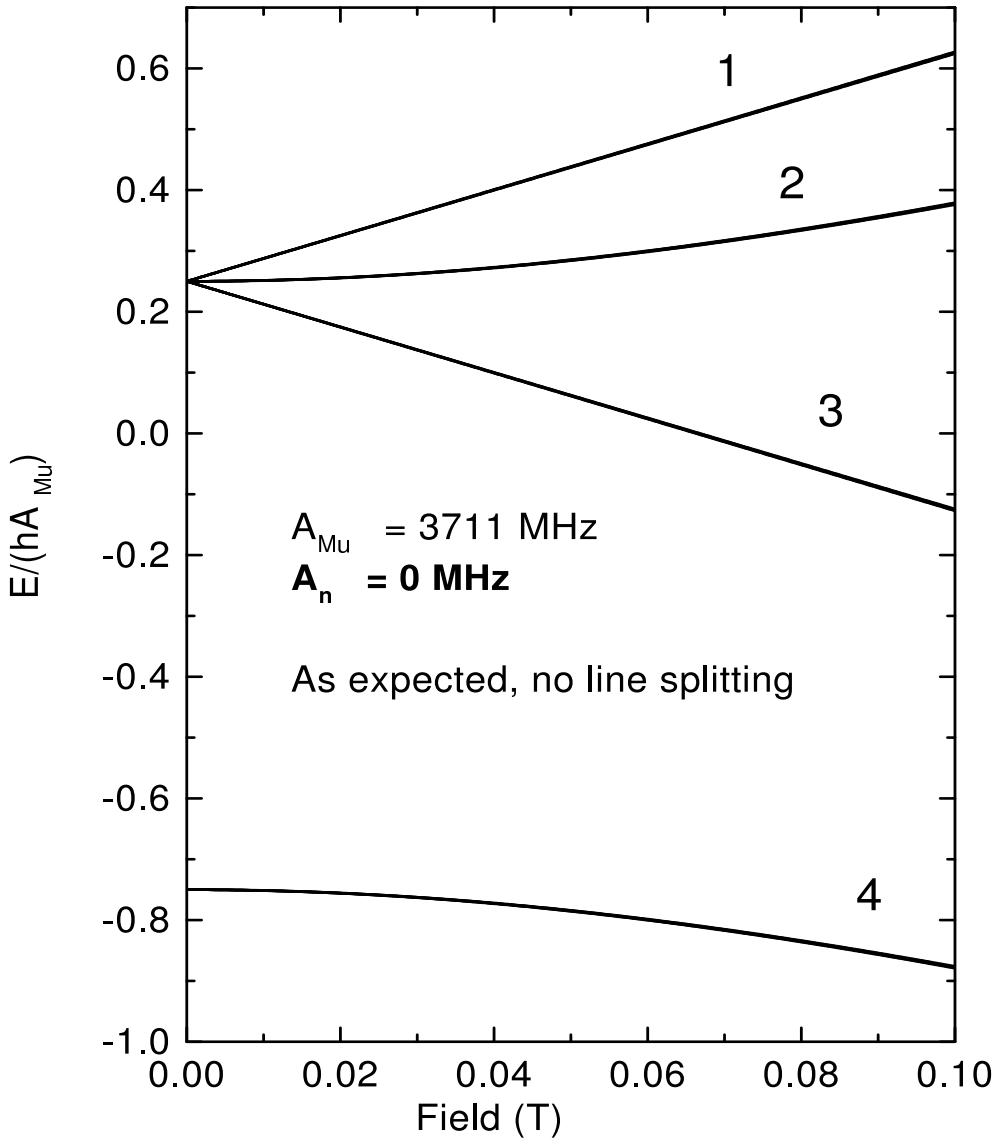

Figure 2.1: The hyperfine energy-level (Breit-Rabi) diagram for isotropic 1s-Mu as a function of magnetic field, where $A_n = 0$.

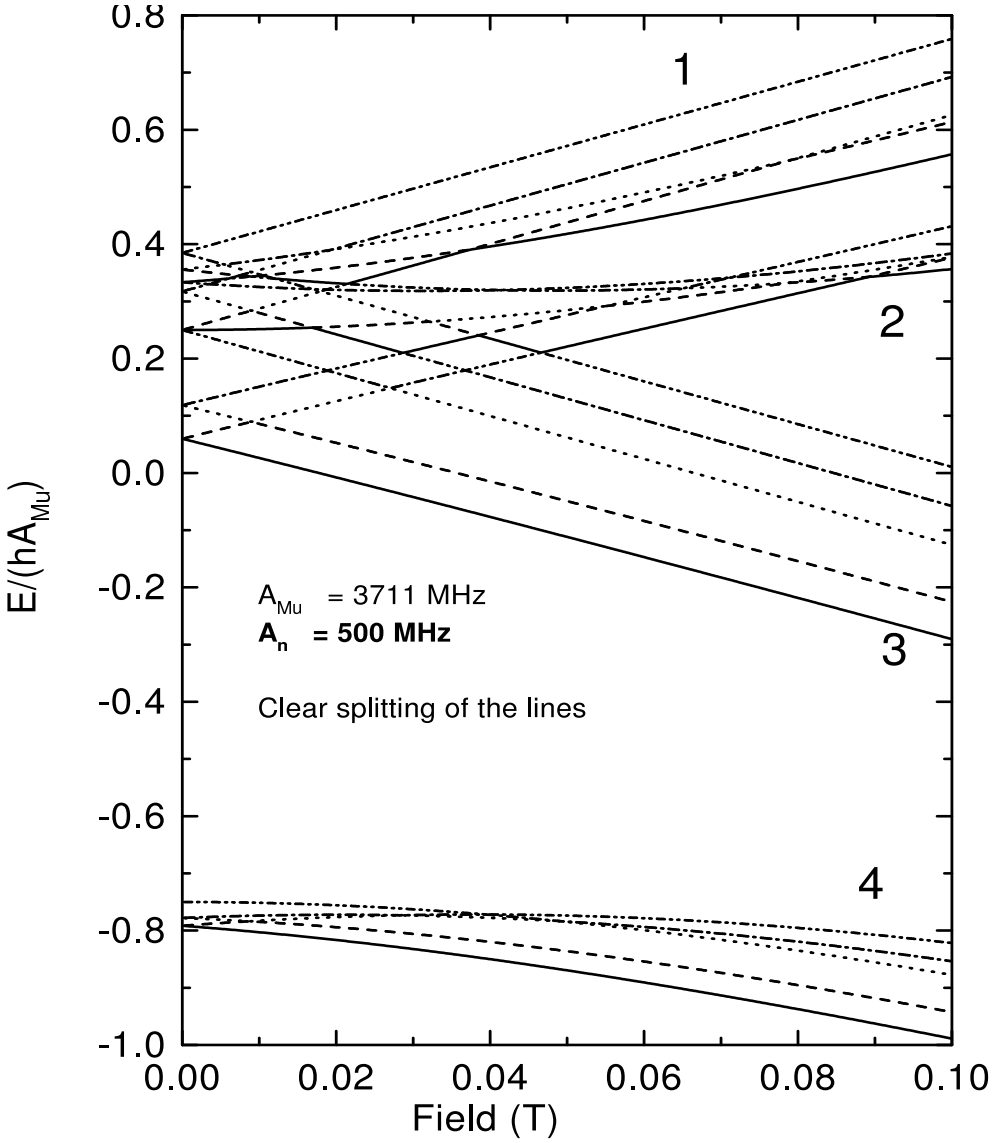

Figure 2.2: The hyperfine energy-level (Breit-Rabi) diagram for isotropic Mu interacting with four neighboring spin 1/2 nuclei of ^{13}C atoms as a function of magnetic field, where $A_n = 500$ MHz.

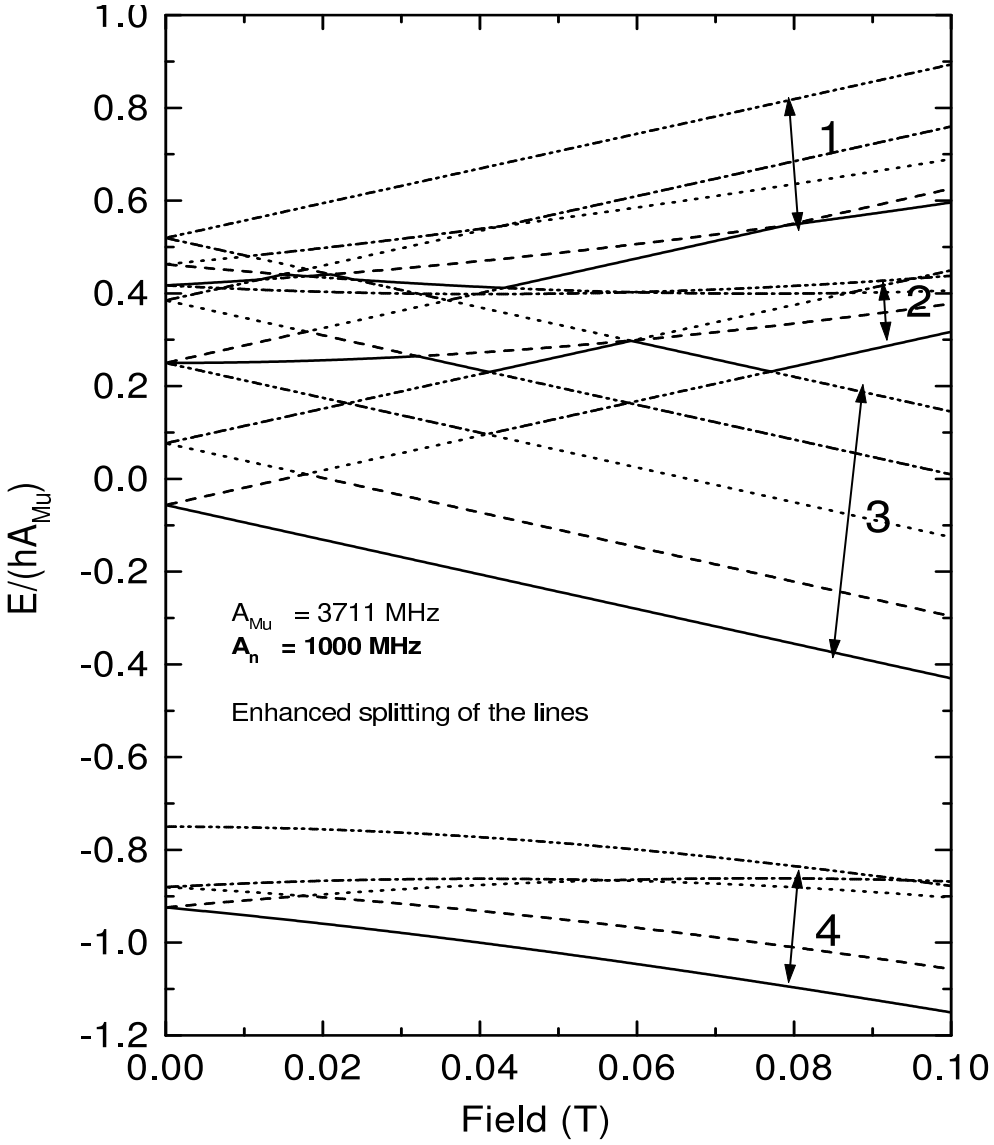

Figure 2.3: The hyperfine energy-level (Breit-Rabi) diagram for isotropic Mu interacting with four neighboring spin 1/2 nuclei of ^{13}C atoms as a function of magnetic field, where $A_n = 1000$ MHz.

form,

$$\rho(t) = \frac{1}{4}\big[1 + \bar{P}_\mu(t) \cdot \bar{\sigma}_\mu + \bar{P}_e(t) \cdot \bar{\sigma}_e + \sum_{j,k} P^{jk}(t)\sigma_\mu^j \sigma_e^k\big], \tag{2.6}$$

where

$\bar{P}_\mu(t) = Tr\big(\rho(t)\sigma_\mu\big)$

$\bar{P}_e(t) = Tr\big(\rho(t)\sigma_e\big)$

$P^{jk}(t) = Tr\big(\rho(t)\sigma_\mu^j \sigma_e^k\big)$,

is used for the spin system consisting of the time-dependent muon, electron, and mixed polarizations, respectively [34]. Assuming (for the density matrix at time 0) that in forming muonium the muon binds electrons of each spin direction with equal probability and that the initial electron and mixed polarizations are zero, it then follows that expression

$$\rho(0) = \frac{1}{4}\big[1 + \bar{P}(0) \cdot \bar{\sigma}_\mu\big] \tag{2.7}$$

is obtained from Equation 2.6. The time evolution of the density matrix is governed by the equation of motion

$$i\hbar\frac{d\rho}{dt} = \big[H, \rho(t)\big], \tag{2.8}$$

which may formally be integrated to yield $\rho(t)$. Upon substituting the results in the time dependent muon polarization vector, discussed in the second term of Equation 2.7, this yields the muon polarization [34],

$$\begin{aligned} \bar{P}_\mu(t) &= \frac{1}{4}\sum_{n,m}\langle n|\bar{P}_\mu(0)\bar{\sigma}_\mu|m\rangle\langle m|\bar{\sigma}_\mu|n\rangle\exp(i\omega t) \\ &= \sum_{n,m} a_{nm}\exp(-\lambda_{nm}t)\cos(\omega_{nm}t + \varphi_{nm}), \end{aligned} \tag{2.9}$$

where $|n\rangle$ and $|m\rangle$, in Equation 2.9, are eigenfunctions given by $|n\rangle = \sum_i a_{ni}|\chi_i\rangle$, with χ_i being the basis spin states and a_{ni} the precession amplitudes. The expansion coefficients $a_{nm} = \langle n|m\rangle$ (the precession amplitude for the muons), λ_{nm} is the depolarization rate of the muon spin, and φ_{nm} is the phase of the muon (with respect to the detector that detects a corresponding decay positron). Equation 2.9 holds both in the presence and the absence of dissipative dynamics.

On the other hand the interpretation of the longitudinal field (LF) measurements of the muonium spin relaxation rate (T_1^{-1}) is based on the notion that the nuclear hyperfine interactions may be treated as an effective magnetic field acting on the muonium's electron. Muonium diffusion causes fluctuation of this effective field which induce transition between the coupled spin states of the electron and muon. The muonium motion against a background of local spins is therefore equivalent to illumination of the Mu with a RF irradiation with a "noise"-like frequency spectrum. The resultant muon depolarization is revealed in the forward-backward asymmetry of the muon decay. Such measurements allow values of $\tau_{\rm c}^{-1}$ and $\delta_{\rm ex}$ to be determined independently. A general expression involves various transitions between the coupled spin states but a reasonable approximation can obtained by assuming dominance of the lowest frequency transition (within the muonium triplet spin states), leading to the expression,

$$T_1^{-1} = \Big(1 - x/\sqrt{1+x^2}\Big)\frac{2\delta_{\rm ex}^2\tau_{\rm c}}{1+\omega_{12}^2\tau_{\rm c}^2} \approx \frac{2\delta_{\rm ex}^2\tau_{\rm c}}{1+\omega_{12}^2\tau_{\rm c}^2}, \tag{2.10}$$

where, $x = 2\Gamma_+ B/\omega_0$, $\Gamma_\pm = \frac{1}{2}\big(g_e\mu_{\rm B} \pm g_\mu\mu_\mu/\hbar\big)$, $\omega_0 = 2\pi A_{\rm Mu_T}$ and $\omega_{12} = \gamma_{\rm Mu}H$ is the muonium intra triplet transition frequency in the magnetic field ($\gamma_{\rm Mu}/2\pi$ = 1.4012 MHz/G) [35,54]. This approach is restricted to the limit of relatively high

longitudinal fields. However, the effective magnetic field approximation is valid only if $\gamma_e H \gg \delta_{\rm ex}$ where γ_e is the electron gyro-magnetic ratio. Moreover, in the limit of slow muonium hopping and high magnetic field, T_1^{-1} is generally too slow (see Equation 2.10) to be measured by the standard μSR technique. These LF measurements, which are very sensitive to muonium dynamics in the fast fluctuation regime, are rather ineffective for the study of very slow dynamics. This theory was used in the extraction of the spin relaxation rates, prompt fractions and nuclear hyperfine interactions from the experimental data.

Chapter 3

Experimental Considerations : Muon Spin Rotation/Relaxation (μSR)

The measurements consist of Transverse Field muon Spin Rotation (TF-μSR) and Longitudinal Field muon Spin Relaxation (LF-μSR). In these techniques, specially constructed equipment, accelerated beams, sophisticated instrumentation, and highly automated computer-controlled data acquisition systems are used. Finally, data analysis and interpretation via simulation of the experiment observables (based on both classical and quantum diffusion models) are carried out.

3.1 Fundamentals of the TF-μSR technique and data analysis

This technique involves a highly polarized beam of muons (implanted into the sample) which enables the determination of the configurations and interaction of muonium in diamond. In this technique the sample was located in an external magnetic field that was perpendicular to the muon spin polarization. The TF-μSR measurements were obtained using the equipment located at the Paul Scherrer Institute (PSI) in Villigen, Switzerland. The equipment included the General Purpose Spectrometer (GPS) and the Low Temperature Facility (LTF) as well as other sections of the beam line as shown in Figure 3.1 The fundamental principle regarding the

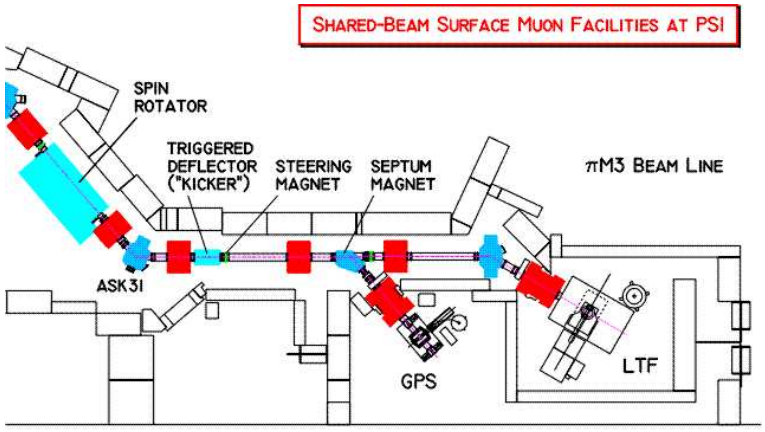

Figure 3.1: Layout of the surface Muon Facility at Paul Scherrer Institute (PSI). Shown in the layout is the Spin Rotator, Triggered deflector "Kicker", Steering magnet, Septum-Magnet, GPS, and LTF.

production of the muon beam at Paul Scherrer Institute (Switzerland) is briefly

outlined below. μSR requires low energy muons that will stop in the sample to be studied. Low energies are available in the required intensities from ordinary two-body pion decay. Thus one must produce sufficient numbers of pions from collisions of high-energy protons (>500 MeV) with the nuclei of the primary target M* such as carbon or beryllium, $p + p \rightarrow \pi^+ + p + n$. The charged pions that are produced, inside the primary target experience energy loss by a thermalization process. The life-time of the free charged pions is 26 billionths of a second and some pions decay at rest near the surface of the primary target. They decay into a muon and muon neutrino, $\pi^+ \rightarrow \mu^+ + \nu_\mu$. The muons have an initial momentum up to 29.8 MeV/c and a kinetic energy up to 4.20 MeV, in the rest frame of the π^+. These muons are collected by a magnetic field and transported in a beam line before entering the samples that were mounted in the GPS and LTF instruments. The pions decayed via the weak interaction, and the conservation of helicity in the process leads to the production of highly spin polarized muons (see Figure 3.2). Pion decay is a two body decay, which implies that the muon and neutrino (ν_μ) are co-linearly emitted. Because the neutrino is only produced with negative helicity (spin anti-parallel to momentum) and anti-neutrino only with positive helicity, the simultaneous conservation of linear and angular momentum forces μ^+ also to have negative helicity in the rest frame of pion. Thus muons, produced from pions decaying at rest, are also 100% polarized, an advantage of the μSR technique.

The Spin Rotator, Electromagnetic Separator (Septum-Magnet) and instruments (GPS and LTF), are permanently installed in the πM3 area where the πM3 beam line transports muons to the sample under investigation (see Figure 3.1). The spin rotator allows the muon spin direction to be rotated into the direction of the muon's

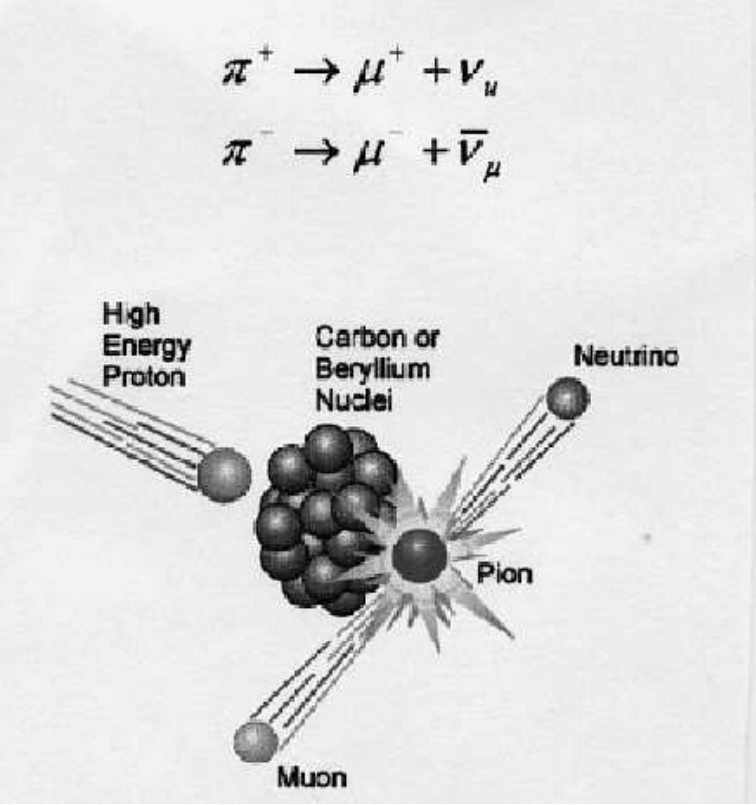

Figure 3.2: Schematic representation of co-linear decay of pions (π^+) into muons (μ^+) and neutrino (ν_μ) in the rest frame of the pion.

momentum. The septum magnet separates the muons in each instrument, i.e GPS or LTF, by only allowing one muon at a time to enter the instrument. The System is known as Muons on request (MORE).

The GPS and LTF instruments were used in acquiring data for high purity single crystal diamond samples. The samples were synthesized in a high temperature high pressure (HTHP) environment from enriched ($> 90\%$) ^{13}C source material. The samples had dimensions of $5.0 \times 5.0 \times 3.5$ mm^3 and $3.5 \times 3.5 \times 3.0$ mm^3, respectively. The measurements were conducted at temperatures ranging from 11 mK to 1.1 K in the LTF and the ranging from 1.8 K to 320 K in the GPS, at a field of 5 mT. Information about the ^{12}C diamond sample is available in reference [8].

Extracted muons, with an initial kinetic energy of 4.119 MeV before entering the sample, revealed themselves by providing a signal to the START detector M (see Figure 3.3).

The GPS instrument, firstly consisted of a cryostat with a sample holder made of copper (Cu) metal. The copper metal base stand was attached to a cold finger that was in turn attached to the cryostat insert. This sample holder system incorporated a Helium (He) flow tube for sample cooling. A heater was mounted behind the sample, enabling achievement of temperatures above room temperature as well as the temperatures below room temperature to be stabilized when used with the He flow.

Secondly, it consisted of positron detectors. The arrangement of the detectors was Forward, Backward, Up, Down and Right (with respect to the sample looking up-

Up and Down detectors not visible.

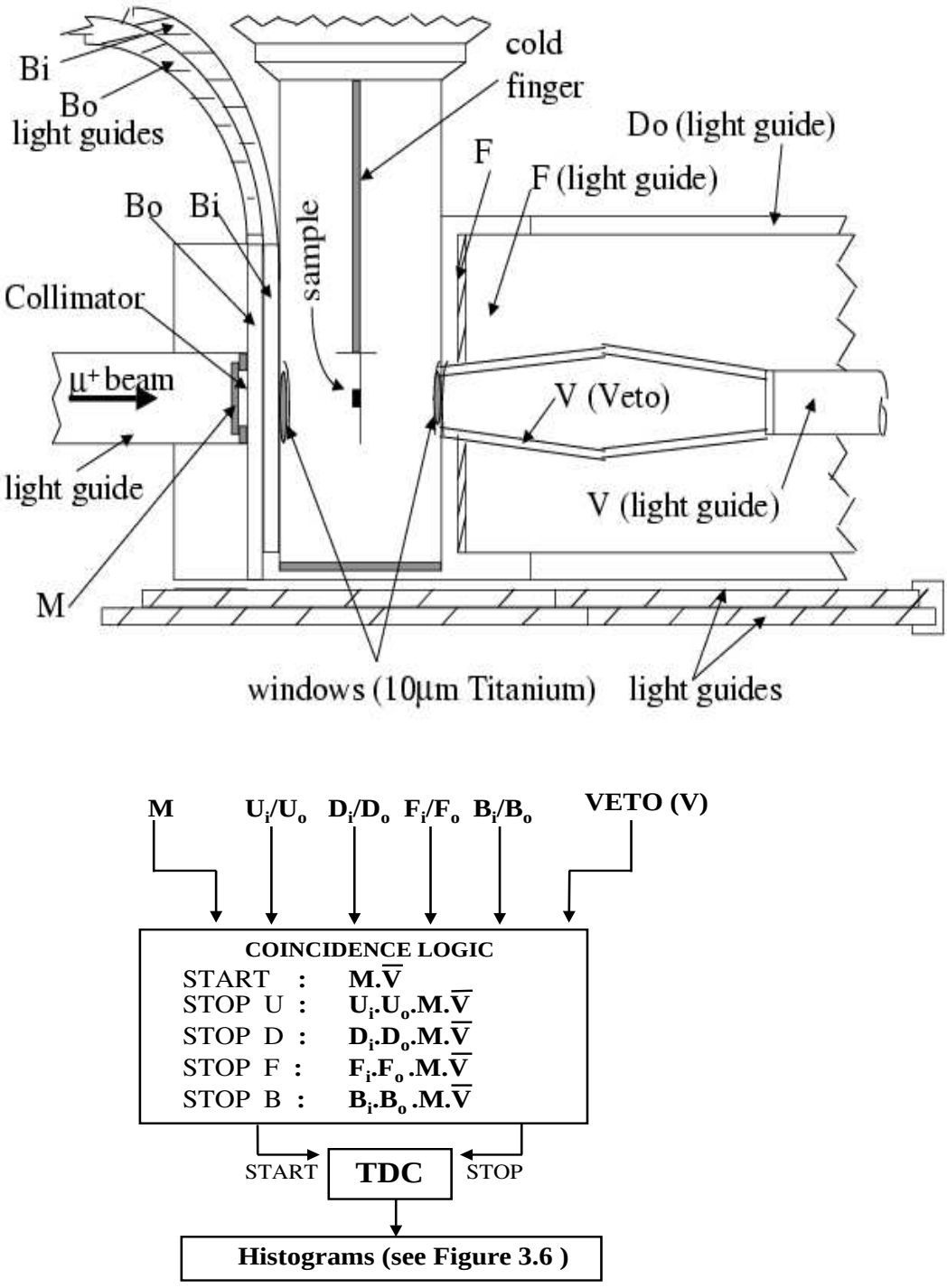

Figure 3.3: Schematic diagram that illustrates the horizontal cross section of the GPS at PSI. A beam of highly polarized muons (μ^+) passed through the collimator and reached the target where μ^+ decay to positron (e^+). Emitted positrons were detected by one of the three detectors. The coincident logic circuit to produce the three time histograms is shown schematically in the lower part of the diagram. TDC is the Time to Digital converter.

stream along the beam). Not all detectors were used, due to the desired experimental setup. Only the Up, Down, Forward and Backward detectors were used as shown in Figure 3.4 . Positron detectors were arranged in an approximately square-shaped

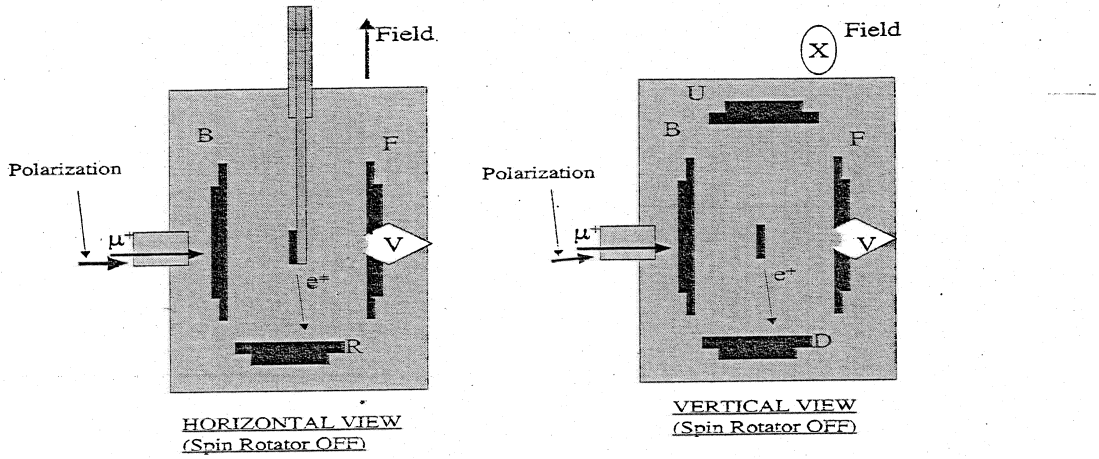

Figure 3.4: Schematic diagram showing the horizontal and vertical view of the General Purpose Spectrometer at Paul Scherrer Institute, without using the spin rotator [30].

arrangement covering three sides of the square. Each of the positron detectors had a pair of scintillator sheets that were coupled to photomultiplier tubes via relatively long light guides. The Veto Cup is found on the axial part of the Forward detector. It (Veto Cup) was designed for samples smaller than the cross section of the muon beam. The logic representation associated with the Veto Cup is represented by $M \cdot \bar{V}$, where the bar line on V shows that no decay positron events should be recorded by the Veto Cup. M denotes the START detector. The signals detected by the Veto Cup are rejected as they correspond to muons that trigger the START detector M,

but later miss the sample. The shape of the Veto Cup is such that it reduces the probability of the positrons exiting the mouth of the cup, after a flypast muon has decayed inside the cup.

In the sample the muons thermalize within a few picoseconds. After thermalization the muon forms well-defined states and becomes associated with an electron as in Equation 2.1 The coupling of the muon to the electron is stronger than the muon to the field. In the presence of an external field, the magnetic moment of an electron (e^-) coupled to the muon precesses in the magnetic field. In turn the muon dances to the tune of the electron. This is due to the fact that the muon has much less magnetic moment compared to that of an electron. During the precession in the sample, the muon decays according to the relation $\mu^+ \rightarrow e^+ + \nu_e + \bar{\nu_\mu}$. The emitted positron ($e^+$) has an anisotropic distribution (see Figure 3.4.), i.e. most positrons (e^+) preferred to be emitted along the direction of the spin of the muon at the instant of decay. The logic representation, showing that the incident muon which had triggered the START detector and later (i.e after a certain time delay) triggered one of the four STOP detectors, is expressed in the form: $\mathrm{U}_i \cdot \mathrm{U}_o \cdot \bar{\mathrm{M}} \cdot \bar{\mathrm{V}}$, $\mathrm{D}_i \cdot \mathrm{D}_o \cdot \bar{\mathrm{M}} \cdot \bar{\mathrm{V}}$, $\mathrm{F}_i \cdot \mathrm{F}_o \cdot \bar{\mathrm{M}} \cdot \bar{\mathrm{V}}$, and $\mathrm{B}_i \cdot \mathrm{B}_o \cdot \bar{\mathrm{M}} \cdot \bar{\mathrm{V}}$ for Up, Down, Forward and Backward respectively, where $i =$ in and $o =$ out (see Figure 3.3).

The positron incident on the scintillator resulted in the production of a light pulse that was conducted along the light guides, towards the photomultiplier where it was converted to an electric pulse which was transported to the electronics room for further processing. The electronic pulse was proportional to the energy loss of the positron as it passed through the scintillator. Each detected positron contributed

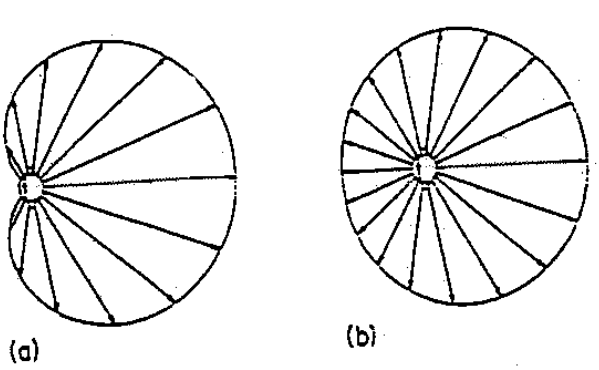

Figure 3.5: Schematic diagram that illustrates the angular distribution of the positrons (e^+) emitted by a decaying muon (μ^+). (a) with maximum energy $m_\mu c^2/2$, and (b) integrated over all energies [25].

to the histogram defined by

$$\begin{aligned} N(t) = B_0 + N_0 e^{-t/\tau_\mu}\Big[1 \;&+\; f_{\mathrm{Mu_T}} \sum_{m,n} a_{m,n}^2 e^{-\lambda_{\mathrm{Mu_T}} t} \cos(\omega_{\mathrm{mn}} t + \varphi) \\ &+\; f_{\mathrm{Mu_{BC}}} \sum_{m,n} a_{m,n}^2 e^{-\lambda_{\mathrm{Mu_{BC}}} t} \cos(\omega_{\mathrm{mn}} t + \varphi) \\ &+\; f_{\mu_{\mathrm{D}}^+} \sum_{m,n} a_{m,n}^2 e^{-\lambda_{\mu_{\mathrm{D}}^+} t} \cos(\omega_{\mathrm{mn}} t + \varphi)\Big] \end{aligned} \tag{3.1}$$

where ω_{ij} and a_{ij} are the precession frequencies and the corresponding amplitudes respectively, calculated from the energy eigenvalues and eigenvectors of the solved spin Hamiltonian of muonium in the presence of spin-1/2 of ^{13}C neighboring nuclei. B_0 is the time-independent background, N_0 is the normalization constant, τ_μ(=2.2 μs) is the muon life-time, φ_{mn} is the phase and $\lambda_{\mathrm{Mu_T}}$ is the spin relaxation rate. The

spin Hamiltonian in the presence of spin-1/2 nuclei is given by

$$\begin{aligned} H_{(\text{Mu+nuclear})} &= hAS_e \cdot S_\mu - \mathrm{g}_e\mu_\mathrm{B} S_e \cdot B - \mathrm{g}_\mu\mu_\mu S_\mu \cdot B \\ &+ h\delta_n \sum_{n=1}^{4} S_e \cdot S_n - \sum_{n=1}^{4} \mathrm{g}_n\mu_n S_n \cdot B, \end{aligned} \tag{3.2}$$

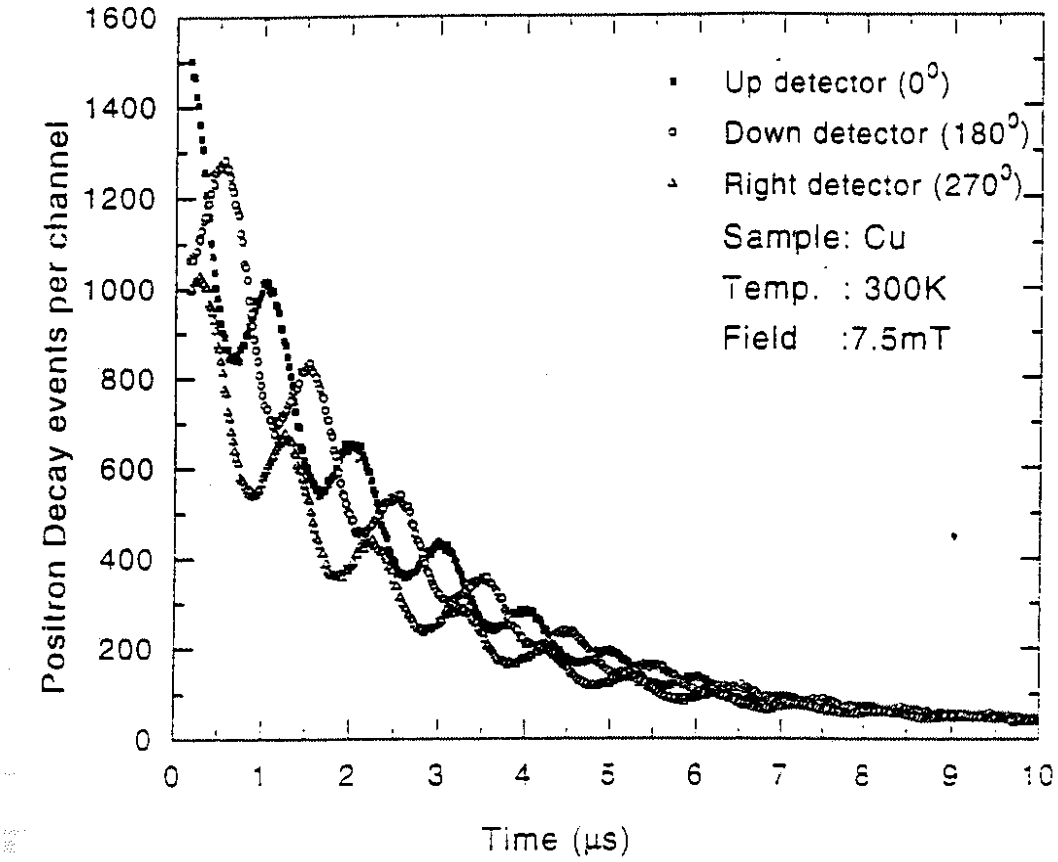

Figure 3.6: Plots of the time histograms (in the three detectors) obtained by measuring the time (in μs units) delay between the muon arrival and decay positron [25].

The asymmetry is obtained from the raw data (see Figure 3.6) by making use of the expression

$$a(t) = \frac{N_{f/u} - \alpha N_{b/d}}{N_{f/u} + \alpha N_{b/d}.} \tag{3.3}$$

The subscripts *f/u* refer to 'forward' or 'up' detectors and similarly *b/d* refer to 'backward' or 'downward' detectors, i.e reduced asymmetry was constructed from opposite detectors. The coefficient $\alpha = \sum N_{f/u} / \sum N_{b/d}$ is close to one if the detectors have similar efficiencies. Theoretical simulations of Equation 3.4 were constructed from Equation 3.1 and fitted to the asymmetry of Figure 3.7.

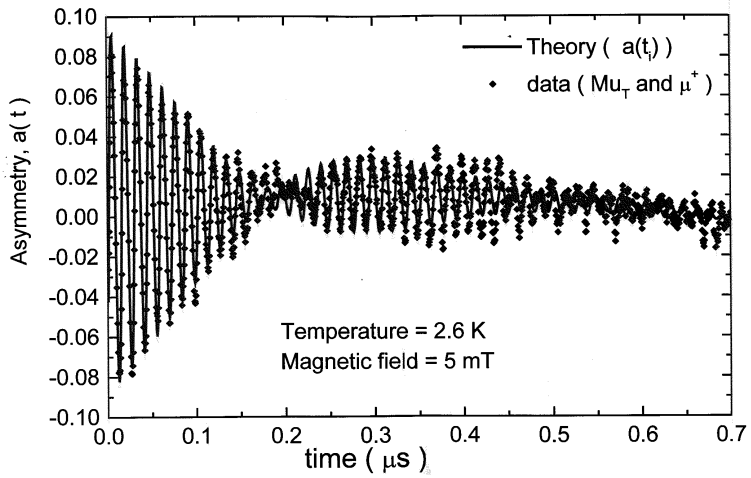

Figure 3.7: The reduced time-dependent asymmetry of the μSR spectra for a ^{13}C diamond.

In time space fits, a Fortran code was used in analyzing the TF-μSR data. The time resolution for the GPS facility was obtained by fitting a Gaussian distribution function

$$a_{abs}(t) = a\ \exp\Big[-\frac{(4\ln 2)t^2}{\delta t^2}\Big] \tag{3.4}$$

to the the prompt peak of the data obtained from the silver sample. In Equation 3.4, a is the (i.e an assumed amplitude if full fraction of the corresponding muon was observed) amplitude of the signal, $a_{abs}(t)$ is the observed amplitude, and δt is the time resolution of the GPS.

The initial formation probabilities (or PAF) were obtained by calibrating the muonium asymmetries with respect to the silver standard. The sum of all initial formation probabilities of the states in diamond, corresponding to a single set of measurements were not equal to unity. This was due to the presence of the so called "Missing Fraction" (MF)

$$f_{missing} = 1 - \frac{1}{A_{\mathrm{Ag}(0)}} \sum_{i=1}^{2} A_i\ , \tag{3.5}$$

where $A_1 = A_{\mu_{\mathrm{D}}^+}$ and $A_2 = A_{\mathrm{Mu_T}}$.

3.2 Fundamentals of the LF-μSR technique and data analysis

The time-differential longitudinal field muon spin relaxation (LF-μSR) experiment was conducted at the ISIS Facility located at Rutherford Appleton Laboratory (ISIS-RAL), in the United Kingdom, using the Implanted Muon Spectrometer known as EMU. The same samples (as used in the TF-μSR measurements) was measured.

Conventional LF-μSR time spectra were recorded at various temperatures, ranging from 10 K to 400 K and at the magnetic fields of 20 mT and 200 mT. The fundamental principle regarding the production of the muon beam is briefly outlined below.

The muon beam was obtained from the 800 MeV proton synchrotron accelerator. Initially, protons are obtained from the source of H^- ions which are produced at an energy of 665 keV and accelerated to 70 MeV before being stripped of their electrons to leave a beam of protons. The protons enter a 52 m diameter synchrotron and are further accelerated up to 800 MeV. These energetic protons bombard a carbon target from which pions are produced (see Section 3.1). Some pions stop in the target near the surface, where they decay "at rest" to form muons that are transported along the beam line. The extracted muon beam, of 4.1 MeV energy, is pulsed with a width of about 28 ns at the position of the EMU spectrometer.

The EMU spectrometer is composed of a set of 16 "forward" and 16 "backward" detectors (see Figure 3.8), where the shown light guides are attached to the detectors. Time-dependent forward-backward asymmetry spectra were constructed from the primary spectra according to the expression (see, for example, [34]),

$$a(t) = a_0 P_z \frac{N_F(t) - \alpha N_B(t)}{N_F(t) + \alpha N_B(t)} \tag{3.6}$$

where N_F(t) and N_B(t) refer to the time-differential muon decay events. $a_0 (\approx 0.24)$ is the maximum experimental asymmetry of the muon decay, and α corrects for different detector efficiencies. Figure 3.9 displays asymmetry decay spectra obtained for muonium in the ^{13}C diamond at a temperature of 220 K and applied longitudinal

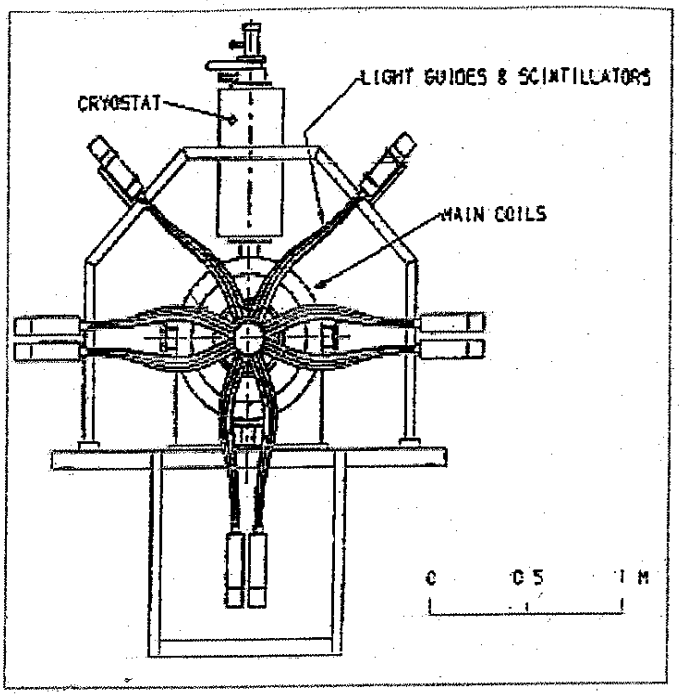

Figure 3.8: Schematic diagram of the EMU spectrometer at ISIS.

fields of 20 and 200 mT. Equation 3.6 was fitted to the similarly manipulated reduced data shown in Figure 3.9 From previous TF-μSR data on the same samples it was

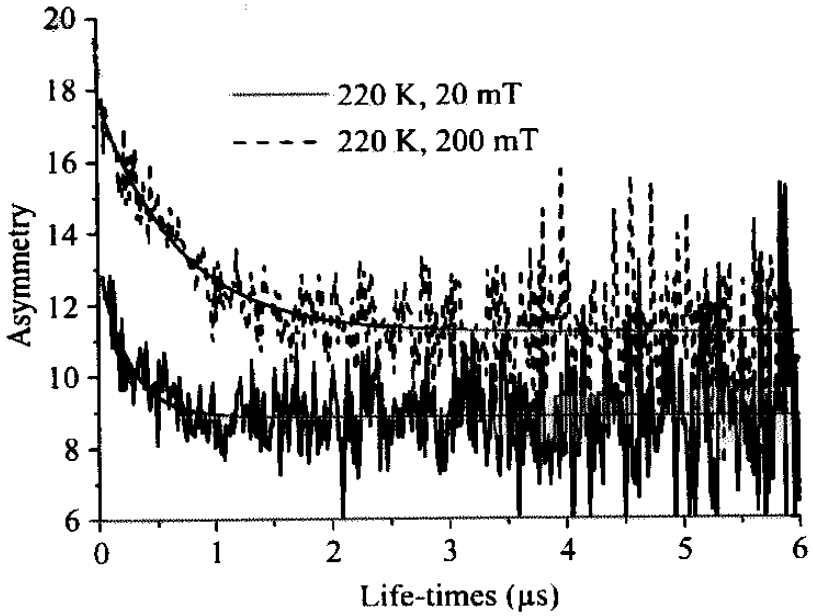

Figure 3.9: Longitudinal field muon decay spectra obtained at the temperature of 220 K and the applied magnetic fields of 20 and 200 mT.

established that the diamagnetic species, μ_{D}^{+}, and the mobile paramagnetic state, $\mathrm{Mu_T}$, would be formed and that the only relaxing species is $\mathrm{Mu_T}$. Therefore the spin relaxation rate, T_1^{-1}, was associated with the mobile $\mathrm{Mu_T}$ state and could be obtained from the time-dependent asymmetry spectra.

Chapter 4

Results and Discussions

The primary objective of this work was to explore the dynamical behavior of the isotropic muonium (Mu_T) in isotopically pure synthetic ^{13}C diamond, using two configurations of the magnetic fields in the muon spin rotation or relaxation experiments. These are Transverse Field muon Spin Rotation (TF-μSR) and Longitudinal Field muon Spin Relaxation (LF-μSR) methods.

In TF-μSR results, two observables, namely the Prompt Absolute Fraction (PAF) and the spin relaxation rate (λ), for both μ_D^+ and the Mu_T states, were obtained. The first observable, namely the PAF, is limited to identification and characterization of μ_D^+ and Mu_T states in the sample, while the λ provides information on the dynamical behavior of the two species in diamond. Subsequent to the TF-μSR experiment, the LF-μSR measurements were conducted on the same ^{13}C diamond sample. The latter focused on further exploration of the dynamical behavior of the

Mu_T state, which was identified as the only relaxing species in TF-μSR method. The main purpose of conducting LF-μSR study was to obtain reliable dynamical information of the Mu_T state in diamond.

4.1 The Muon (μ_D^+) and isotropic muonium (Mu_T) in a ^{13}C diamond, studied using TF-μSR experiment

4.1.1 Prompt formation probabilities of μ_D^+ and Mu_T states

The results of the prompt fractions or formation probabilities (PAF) obtained in the current ^{13}C diamond and those previously obtained in other diamond samples are shown in Table 4.1. In addition to the results of Table 4.1, the PAF for the Mu_T and μ_D^+ states, as function of temperature, are shown in Figure 4.1 where the PAF for the Mu_T and the μ_D^+ states are fairly constant at 73±5% and 4.3±0.5%, respectively, in the temperature range measured. It is noted that, the μ_D^+ state has the lowest PAF compared to the Mu_T state, an indication that an enhanced formation of Mu_T is favored in diamond with a low concentration of nitrogen. This is evident in the results shown in Table 4.1, where the formation of Mu_T in the ^{13}C diamond is consistent with the results obtained in natural type IIa diamond, known to have low concentrations of nitrogen and boron. On the other hand, the Mu_T obtained in the ^{13}C diamond has a larger fraction than those obtained in nitrogen- and boron-

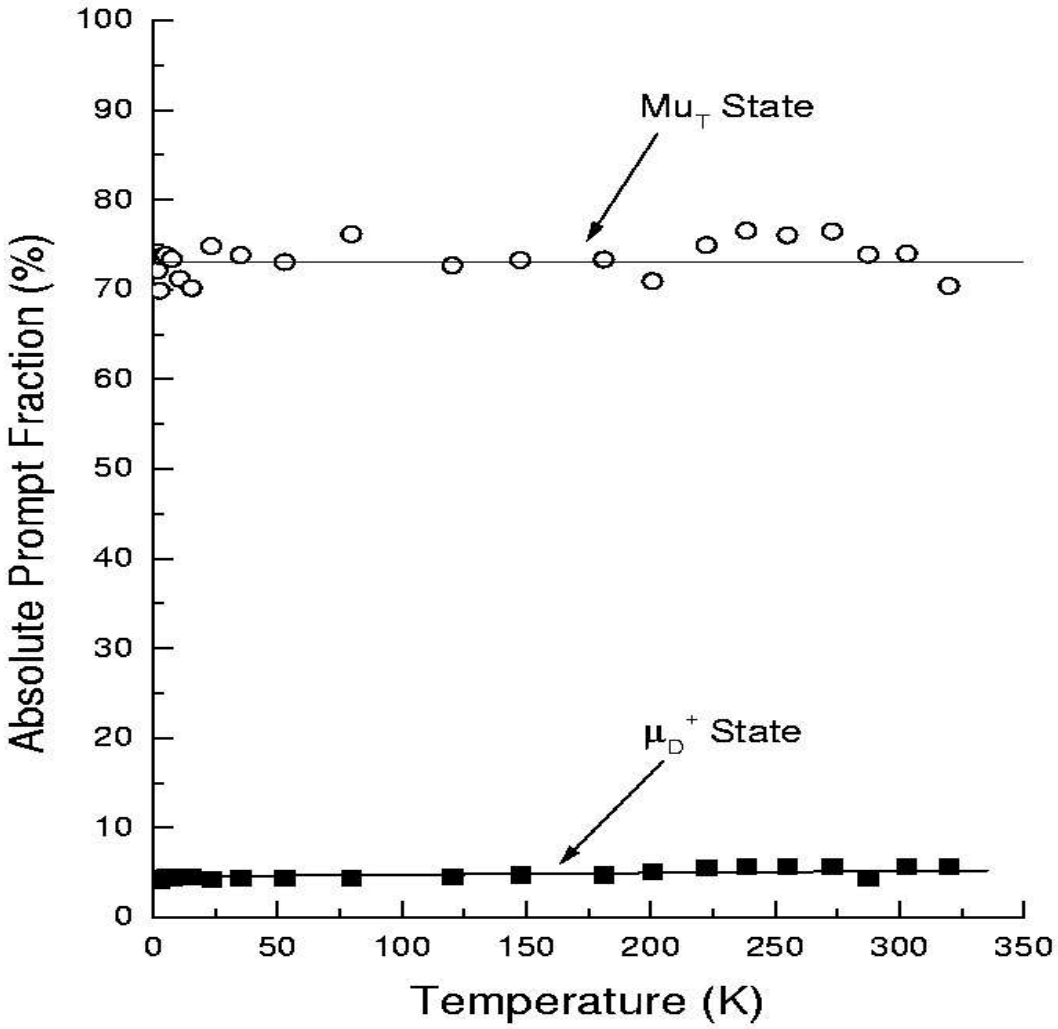

Figure 4.1: Prompt absolute fractions of Mu_T and μ_D^+, as a function of temperature, in the ^{13}C diamond.

rich diamond samples. In fact the Mu_T state obtained in the nitrogen-rich type Ia diamond (with aggregated nitrogen centres) is reduced by about a factor 2. This is attributed to the presence of nitrogen in the diamond.

The prompt fractions of the μ_D^+ state, obtained in all samples are comparable, indicating that their formation is not significantly influenced by the presence of defects or impurities. In each of the six samples, the prompt fractions do not add up to 100%, probably due to the formation of other states that could not be resolved by the μSR spectrometer.

Table 4.1: Comparison of the Prompt Absolute Fractions of the μ_D^+ and the Mu_T states in ^{13}C diamond with those obtained in the previous TF-μSR studies.

Sample	Temp.(K)	$f_{\mu_D^+}$ (%)	f_{Mu_T} (%)	Reference
^{13}C diamond	[0.011, 320]	4.3±0.5	73±5	This work
^{12}C diamond (IIa)	[5, 300]	6±1	61±4	[Smallman 1996]
CVD	10,100,300	5±1	37±4	[Machi 1996]
Nitrogen-rich diamond (Ia)	[5, 270]	4±1	0	[Smallman 1996]
Nitrogen-rich diamond (Ia)	4.2	< 10	20±4	[Holzchuh 1982]
Boron-rich diamond (IIb)	[5, 300]	[10, 28]	<55	[Smallman 1996]
Undoped diamond(IIa)	Low temperatures	8.1±3.0	68.9±1.0	[Patterson 1988]

4.1.2 Dynamical behavior of μ_D^+ and Mu_T

The experimental values of λ_{Mu_T} in the synthetic ^{13}C diamond sample are presented in Figure 4.2. Also, shown in the figure is the data of the Mu_T in a ^{12}C diamond [31], deliberately spiked with about 1 ppm of mono-vacancies. In general the interpretation of the dynamical behavior of the Mu_T in TF-μSR configuration depends on the nature of the dephasing mechanism. In the current ^{13}C diamond two modes are considered; namely "relaxation by deep trapping after fast diffusion" and "motional narrowing". The former mode is appropriate for a sample with deep traps, such as in the pure ^{12}C diamond with mono-vacancies [31] where the Mu_T traps deeply at vacancies after rapid diffusion. Each member of the Mu_T ensemble has different arrival time at the trap and once trapped each Mu_T state precesses at a different frequency and the ensemble eventually dephases. In this mode faster diffusion leads to larger relaxation of the spin polarization. The latter mode is appropriate for shallow traps, such as in the current ^{13}C diamond sample where the motion of the Mu_T is against a background of randomly oriented nuclear spins. A static or trapped Mu_T ensemble experiences different local fields and each member of the ensemble precesses at a slightly different rate, leading to the relaxation of the spin polarization of the Mu_T ensemble. If the Mu_T state is sufficiently mobile, such that it averages the local field to a single well-defined value on a time scale, which is short compared to the period of its precession, then the ensemble does not dephase. In this mode, faster diffusion leads to smaller relaxation rate of the spin polarization. This indicates that in an isotopically pure ^{13}C diamond, the spin relaxation rate of the Mu_T signals would be small in the motionally averaged interaction between the Mu_T and the nearest nuclear moments. Both mechanisms discussed above could

be present simultaneously if there were some deep traps (mono vacancies) present in the ^{13}C sample. In this work dynamical information was obtained through the dominant T_2 relaxation mechanism (also known as spin-lattice interaction) where both ^{12}C and ^{13}C data exhibit temperature independent $\lambda_{\mathrm{Mu_T}}$ below 200 K. Above 200 K, $\lambda_{\mathrm{Mu_T}}$ decreases (or increases) as temperature increases in a ^{12}C (or ^{13}C) sample (see Figure 4.2). Of most significance in both data sets is that an increase or a decrease of $\lambda_{\mathrm{Mu_T}}$ follows a single power law which is consistent with theoretical predictions for quantum diffusion of light interstitials in condensed matter [31, 36]. The diffusion modes, applicable to the data of Figure 4.2, are briefly outlined in different temperature regimes by Storchack and Prokof'ev 1998 [33] and are discussed in accordance with Figure 4.3. At low temperatures, below about a tenth of the Debye temperature (Θ_{D}), the interstitials could be in the band-like (Bloch) state, i.e undergoing coherent tunneling. As the temperature increases, but still below a tenth of Θ_{D}, phonon destruction of the band occurs, which lowers the diffusion constant. Initially, the phonon scattering is dominated by two-phonon process where phonon scattering has a net elastic nature.

The two-phonon assisted tunneling could be understood by imagining that the $\mathrm{Mu_T}$ is localized in the tetrahedral site (T-site) which acts as a shallow trap locally distorting its environment, forming a slightly deeper trap. This situation is known as the self-trapped polaron which would not tunnel coherently to the neighboring T-site before the appropriate distortion of that site. Therefore the energy levels for the $\mathrm{Mu_T}$ in the distorted and undistorted potential wells are not in resonance. In order to achieve resonance, the first phonon distorts the neighboring T-site so that it comes into resonance with the occupied T-site (see Figure 4.4). Then, the $\mathrm{Mu_T}$

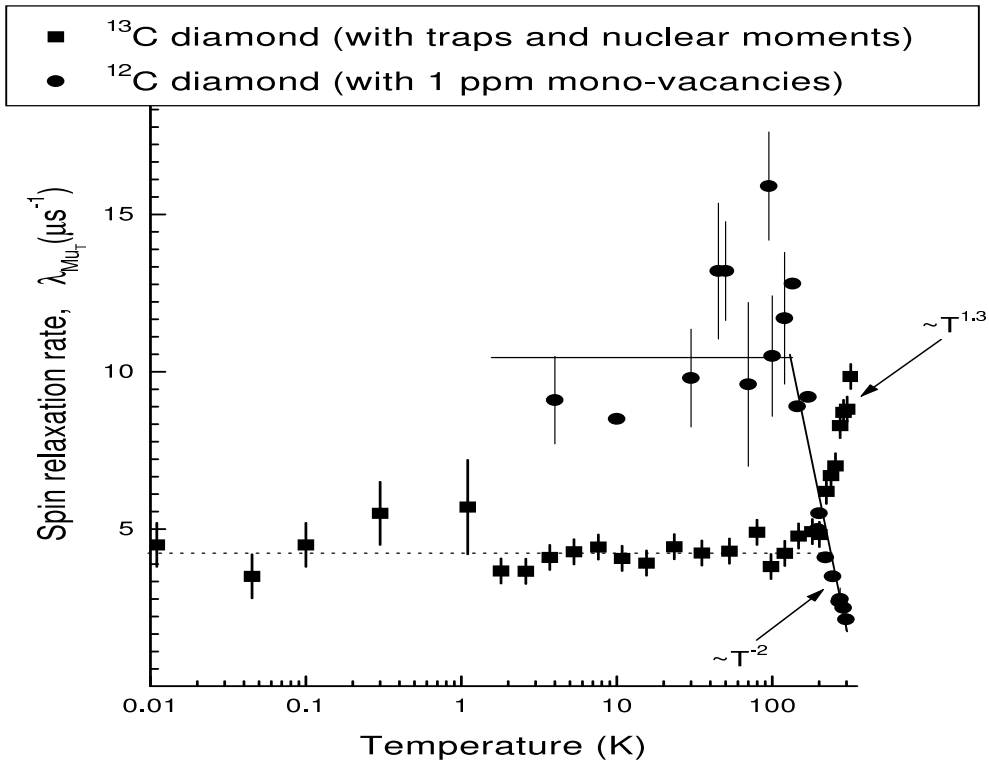

Figure 4.2: Spin relaxation rate of the Mu_T state in temperatures ranging from 11 mK to 320 K. The applied magnetic fields of 5 mT and 7.5 mT were used for the ^{13}C and ^{12}C diamond samples, respectively.

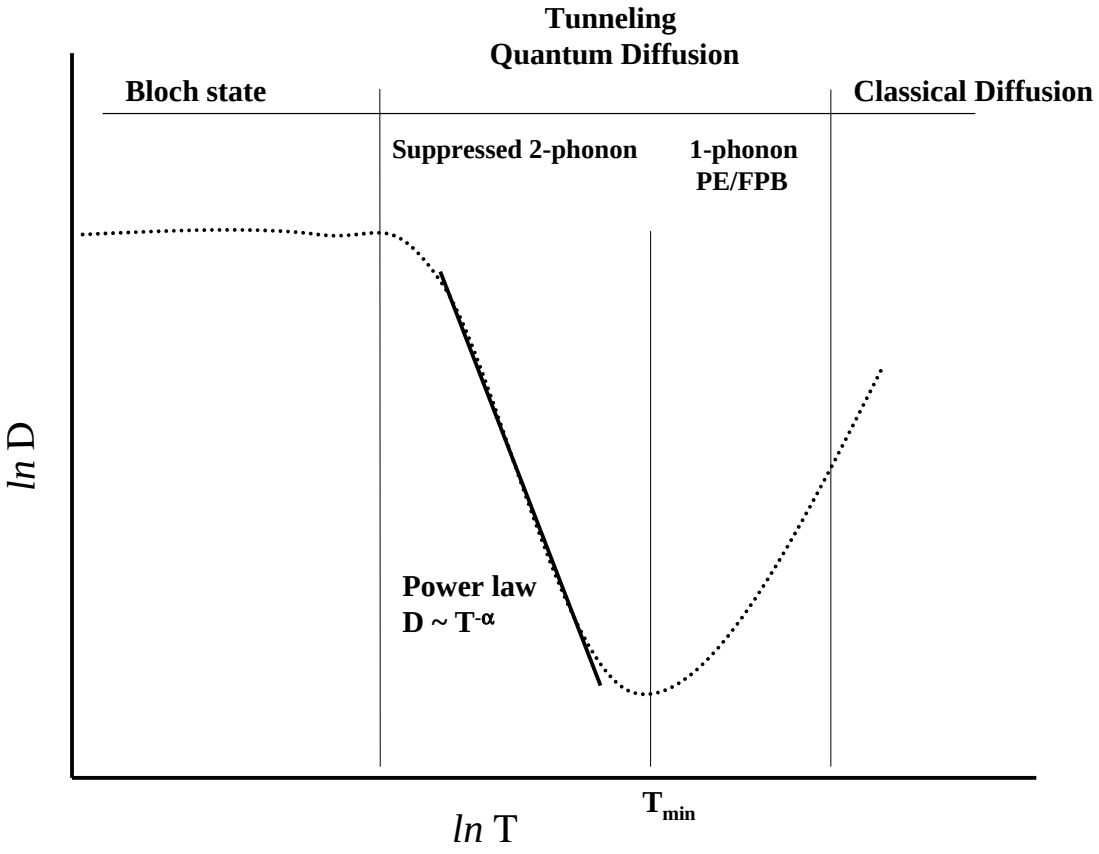

Figure 4.3: Schematic diagram of various motion of muonium in diamond.

could tunnel across coherently. The second phonon represents the collapse of the originally occupied T-site to its undistorted state. In Figure 4.3, coherent motion

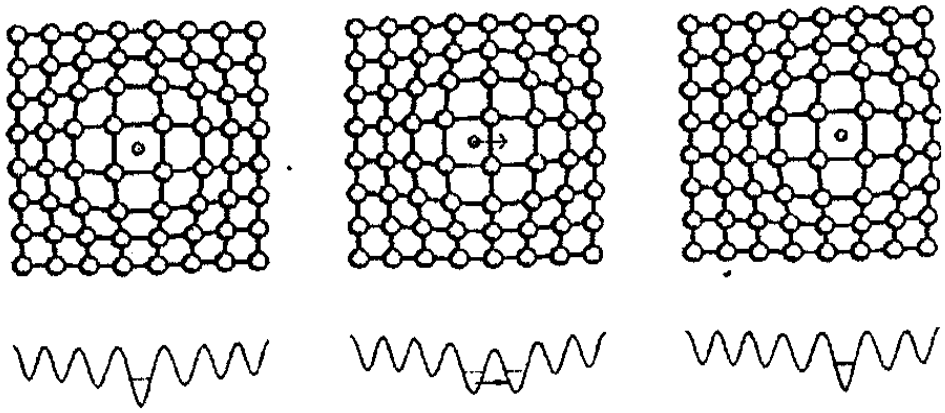

Figure 4.4: Schematic diagram that illustrates diffusion by phonon-assisted tunneling [36].

is suppressed with increasing temperature as phonons become more prolific. The dependence on the temperature of the diffusion constant in this region is of the form $D \propto T^{-\alpha}$ for $2 < \alpha < 9$, where the exponent α is determined by details of the unit cell and the phonon spectrum. The diffusion constant diminishes with increasing temperature in the phonon suppressed regime, until it reaches a minimum. At temperatures in the vicinity of a tenth of Θ_{D}, lattice thermal excitations are expected to result in the incoherent one-phonon mechanism. At the temperature above a tenth of Θ_{D} the one-phonon mechanism is described by the polaron effect (PE) and the fluctuational preparation of the barrier (FPB) effect.

This could be understood by considering a charge carrier that is fixed at a given position in a solid. The presence of the additional (stationary) charge would gen-

erally act as a substantial perturbation on its immediate environment, producing a displacement of atoms in its immediate vicinity and causing a reduction in the total energy of the system. The equilibrium positions which these atoms would assume in response to the added charge will be such as to produce a potential well for the carrier. In fact if the potential well associated with the local lattice distortion is sufficiently deep, the carrier will occupy a bound state, being unable to move without an alteration of the positions of the neighboring atoms. The unit comprised of the localized charge carrier and its concomitant atomic deformation is termed a small polaron when the carrier is essentially confined to a single atomic site. Clearly a small polaron can only be expected to form if an excess charge carrier will move sufficiently slowly so as to linger at a particular atomic for time ample to permit the surrounding atoms to adjust to its presence. These two effects interfere with each other. However, the FPB dominates leading to an increase of the diffusion constant with increasing temperature. Finally, when the temperature reaches the zero-point energy of the Mu_T state in the trap, the motion evolves to classical Arrhenius over-barrier hopping. From the discussion regarding the mechanism of observing quantum diffusion, it becomes evident that the spin relaxation rate, λ_{Mu_T}, in the ^{13}C and ^{12}C diamonds (see Figure 4.2) would be the inverse of the diffusion constant for the "motional narrowing" mechanism in ^{13}C diamond, and proportional to the "relaxation by deep trapping after diffusion" mechanism in diamond with mono-vacancies, respectively.

In the ^{12}C diamond, the large λ_{Mu_T} below 200 K is associated with fast quantum diffusion of the Mu_T state, that enables the Mu_T state to reach vacancies over relatively short times compared to higher temperatures (above 200 K) where

multi-phonon scattering hinders diffusion. The decrease of $\lambda_{\mathrm{Mu_T}}$ with an increase in temperature follows a weak power law $\sim T^{-2}$ which is attributed to unaccounted temperature dependence of the trapping radius of mono-vacancies. It follows that there is a clear indication that the $\lambda_{\mathrm{Mu_T}}$ is a mixture of two depolarization mechanisms in the ^{13}C diamond; namely the obvious less dominant trapping of $\mathrm{Mu_T}$ state at some intrinsic vacancies as well as the dominant interaction with nuclear magnetic moments of ^{13}C atoms. In the presence of only the nuclear magnetic moments, as the dephasing mechanism, the $\lambda_{\mathrm{Mu_T}}$ would have been much less than the current value of about 4 $\mu\mathrm{s}^{-1}$ (obtained below 200 K), and this would have been mainly attributed to the motionally averaged interaction between the $\mathrm{Mu_T}$ and the nearest nuclear magnetic moments of ^{13}C atoms. There would have been a strong positive power law $\sim T^7$ above 200 K, as predicted by the theory of quantum diffusion of light interstitials in condensed matter.

The weak power law in the data of ^{13}C diamond could be explained by considering the schematic curves of Figure 4.5, where curves 1 and 3 resemble $\lambda_{\mathrm{Mu_T}}$ that would have been obtained if only one of the earlier mentioned dephasing mechanisms was present at a time. In the presence of both mechanisms, curve 2 (a combination of curves 1 and 3) would be obtained if curve 3 is stronger than curve 1, as is suspected to be the case in the current ^{13}C data, a relatively large temperature independent $\lambda_{\mathrm{Mu_T}}$ ($\approx 4\mu\mathrm{s}^{-1}$) below 200 K and the weak positive power law ($\sim T^{1.3}$) above 200 K would be obtained. The decrease of $\lambda_{\mathrm{Mu_T}}$ with a decrease in temperature above 200 K, in the ^{13}C diamond demonstrates the motional narrowing of the $\mathrm{Mu_T}$ state, i.e the $\mathrm{Mu_T}$ diffuses faster as the temperature decreases. This fast diffusion is promoted quantum diffusion mechanism in the lower temperature regime. In addition,

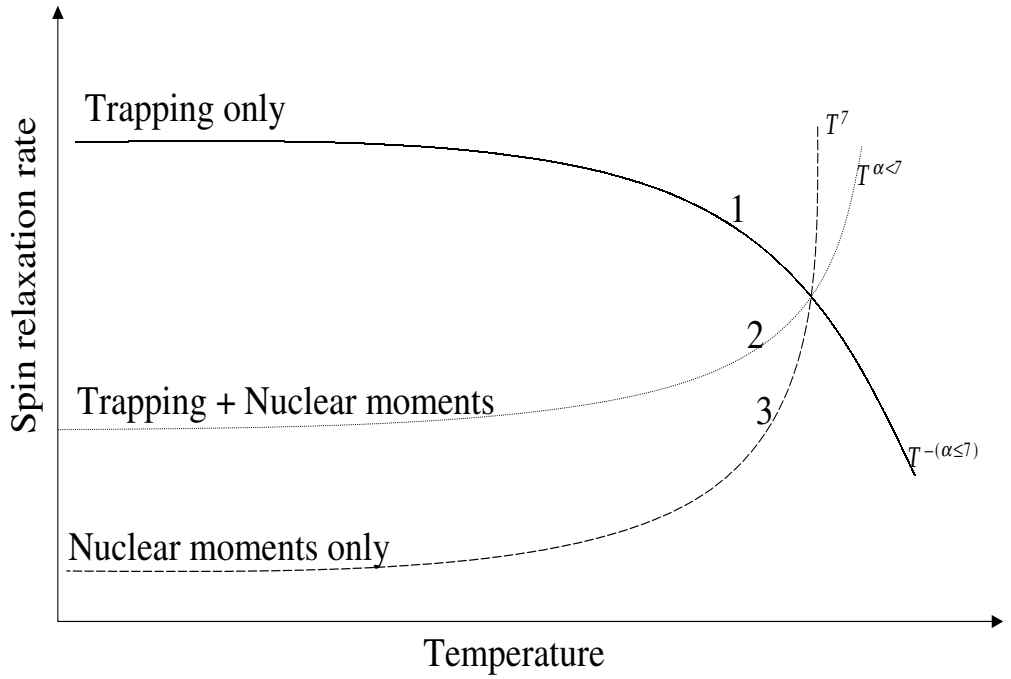

Figure 4.5: Schematic diagram that illustrates the effect, on the spin relaxation rate, of having a combination of nuclear magnetic moments and traps as spin's dephasing mechanisms in condensed matter. In the diagram, the mixture of curves 1 and 3 result in curve 2, which resemble data of a ^{13}C diamond (see Figure 4.2).

the onset of the two-phonon to one- and multi-phonon transitions begins just below 200 K, consistent with the previously discussed theoretical prediction of a tenth of Θ_D [37], where $\Theta_D \approx 2200$ K for diamond. The mixture of the two dephasing mechanisms in a ^{13}C sample complicates the conversion of the λ_{Mu_T} to the hop rate. No evidence of the diffusion of the diamagnetic state, presumed to be the positive ion immobilized at the bond-centre, could be inferred from its temperature-independent spin relaxation rate $\lambda_{\mu_D^+}$ ($= 0.10 \pm 0.02\ \mu s^{-1}$) in the ^{13}C diamond sample.

In the quest to further understand the dynamical behavior of the Mu_T in a ^{13}C diamond, further investigations were conducted on the same sample using the LF-μSR method where the spin loss is mostly due to interaction with magnetic moments of ^{13}C atoms.

4.2 Dynamical behavior of isotropic muonium (Mu_T) in ^{13}C diamond, studied using LF-μSR experiments

Based on the TF-μSR results of Section 4.1, the LF-μSR measurements were conducted in the same ^{13}C diamond sample, with the aim of a less model dependent analysis of the dynamics experienced in the TF-μSR measurements. In the LF-μSR experiment, the measurements were extended to 400 K in order to explore dynamical behavior of Mu_T to relatively higher temperatures, so as to map out the region of one and multi-phonon mechanisms more clearly.

In the LF-μSR experiment where the T_1 relaxation mechanism (also known as spin-spin interaction) dominates, the mobile muonium state (Mu_T) experiences a fluctuating field due to the local moments of ^{13}C atoms. From the previous TF-μSR data on the same sample it was established that only the diamagnetic state, μ_D^+ ($f_{\mu_D^+} = 4.3 \pm 0.5\%$) and the paramagnetic state, Mu_T ($f_{Mu_T} = 73 \pm 5\%$) are formed. The only relaxing species was found to be the Mu_T [38] and therefore the spin relaxation rate in the LF-μSR, T_1^{-1}, was attributed to the Mu_T and was extracted from the time-dependent asymmetry spectra shown in Figure 4.6. These asymmetry decay spectra were obtained for muon/muonium in the ^{13}C diamond as a function of temperature and the applied longitudinal magnetic fields of 20 mT and 200 mT. It is noted in Figure 4.6. that the spin relaxation rate increases with an increase in temperature. The difference in the two spectra of each figure is due to quenching of the nuclear hyperfine interaction. The solid lines in each spectra were obtained by simultaneous multi-dimensional fitting of the time-dependent muon asymmetry, for different temperatures and magnetic fields, using the Redfield theory described in Kadono (1990) [42]. The following equations were used in the extraction of the relaxation rate and the hop rate.

$$P_z(t) = \exp(-t/T_1(B,T)) + C \tag{4.1}$$

with T_1 defined as

$$T_1^{-1} = \left(1 - x/\sqrt{1+x^2}\right) \frac{2\delta_{ex}^2 \tau_c}{1 + \omega_{12}^2 \tau_c^2} \tag{4.2}$$

The field dependence enters into the expression for the dominant precession frequency,

$$\omega_{12} = \frac{\omega_0}{2}\left[1 + (\Gamma_-/\Gamma_+)x - \sqrt{1+x^2}\right] \tag{4.3}$$

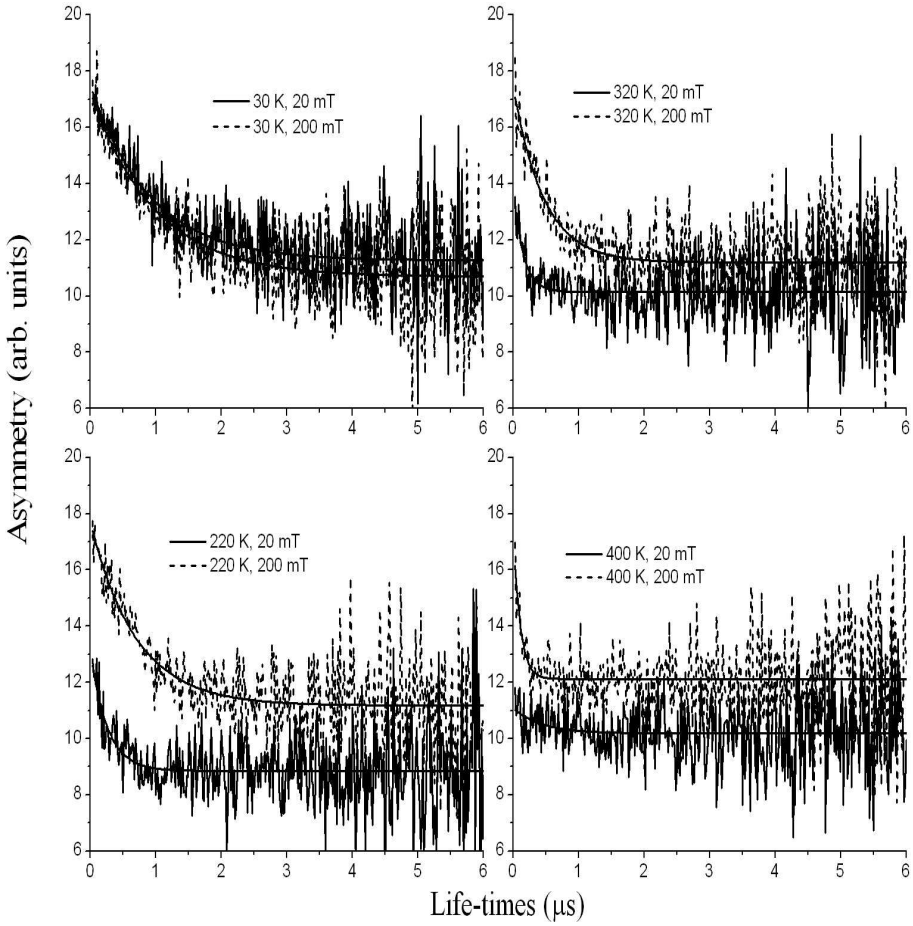

Figure 4.6: Longitudinal field muon decay spectra obtained in the ^{13}C diamond at different temperatures and applied magnetic fields.

The other parameters are $\Gamma_{\pm} = \frac{1}{2}\left(g_e\mu_B \pm g_\mu\mu_\mu/\hbar\right)$, $\omega_0 = 2\pi A_{Mu_T}$ and $x = 2\Gamma_+ B/\omega_0$ where A_{Mu_T} and B are the hyperfine constant and the applied field, respectively. The nuclear hyperfine parameter δ_{ex} sets the time scale of T_1^{-1}. It is a measure of the combined effect of all the nuclear spins, in the vicinity of the Mu_T, interacting with the muon via the correlated electron. The temperature dependence of the hop rate, τ_c^{-1}, and δ_{ex} were therefore extracted in this way. There is not a unique correspondence between T_1^{-1} and τ_c^{-1} unless the fitting is done simultaneously for different magnetic fields. Moreover, the choice of the magnetic fields must be carefully made. To illuminate the choice of the magnetic fields, the dependence of T_1^{-1} on magnetic field for different temperatures was measured and is displayed in Figure 4.7. The

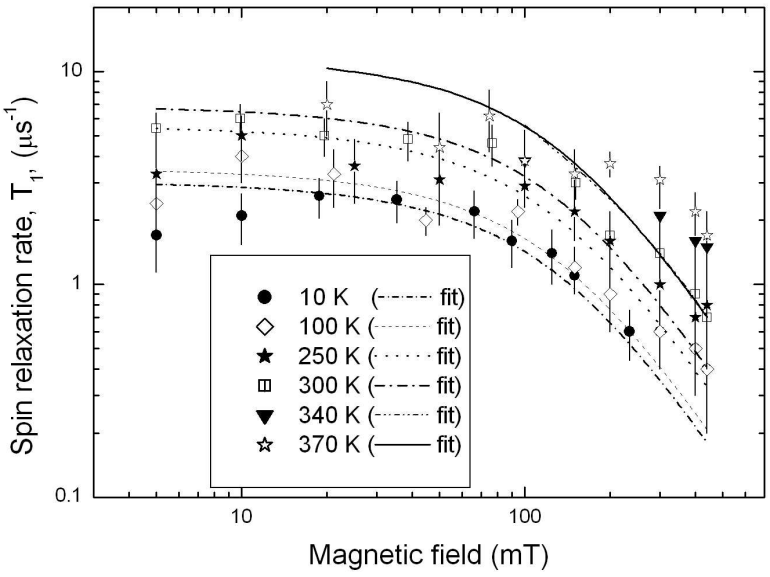

Figure 4.7: Field scans at different sample temperatures of the spin relaxation, T_1^{-1}, of Mu_T in a ^{13}C diamond. The solid and dashed lines represent fits obtained using Equation 4.2.

fields of 20 and 200 mT were selected as these gave substantially different T_1^{-1} values over the temperature range investigated.

Theoretically calculated curves of the same type are shown in Figure 4.8. In contrast

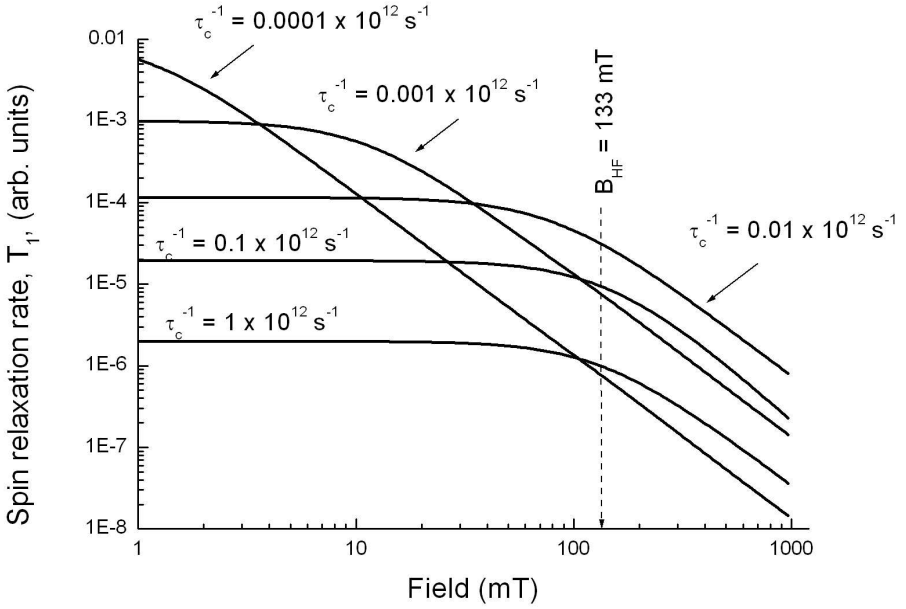

Figure 4.8: Theoretically simulated curves of arbitrary spin relaxation rate, T_1^{-1}, of $\mathrm{Mu_T}$ in diamond as a function of temperature.

to Equation 4.2, where a single transition frequency taken is assumed, these include the contribution of possible transitions between the hyperfine-coupled electron-muon spin states [39]. One notes the existence of the rollover point separating a region of constant values of T_1^{-1} from a region of decreasing T_1^{-1} with increasing temperature. For very large τ_c^{-1}, this rollover point is at the hyperfine field (~ 133 mT) for $\mathrm{Mu_T}$ in diamond. For lower τ_c^{-1}, the rollover point moves to even lower fields. Comparison of our data with these theoretical curves indicates that τ_c^{-1} must be at least larger

than $\tau_c^{-1} \sim 10^{10}$ s^{-1} for all temperatures studied. The extraction of τ_c^{-1} via the Redfield theory (presented below) confirmed this analysis. Note that the magnetic fields chosen were also on both sides of the rollover position.

The spin relaxation rate, T_1^{-1}, of Mu_T at magnetic fields of 20 and 200 mT (as function of temperature) is shown in Figure 4.9. It is noted that T_1^{-1} for both fields

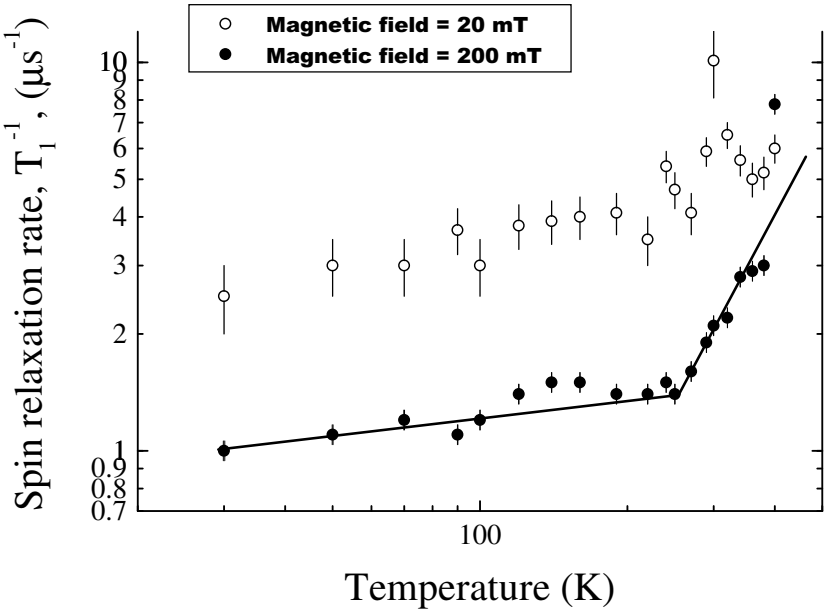

Figure 4.9: Spin relaxation rates, T_1^{-1}, of Mu_T in the ^{13}C diamond as a function of the magnetic fields (20 and 200 mT). Solid line guides the eye.

increases as temperature increases. The curve with the larger field has a lower T_1^{-1} due to the partially decoupled or quenched nuclear hyperfine interaction δ_{ex}. The curve for the larger magnetic field exhibits the power law dependence in T_1^{-1} as is also the case for the Mu_T diffusion studies, performed using TF-μSR [31,38]. However,

one of the important reasons for repeating these studies in the LF-μSR configuration is that the model for the extraction of the hop rate, τ_c^{-1}, is more reliable. The hope rate is the more important quantity for the discussion of quantum diffusion. Redfield analysis of the τ_c^{-1} and δ_{ex} are presented in Figure 4.10 as a function of temperature. The hop rate is essentially constant with a value of approximately

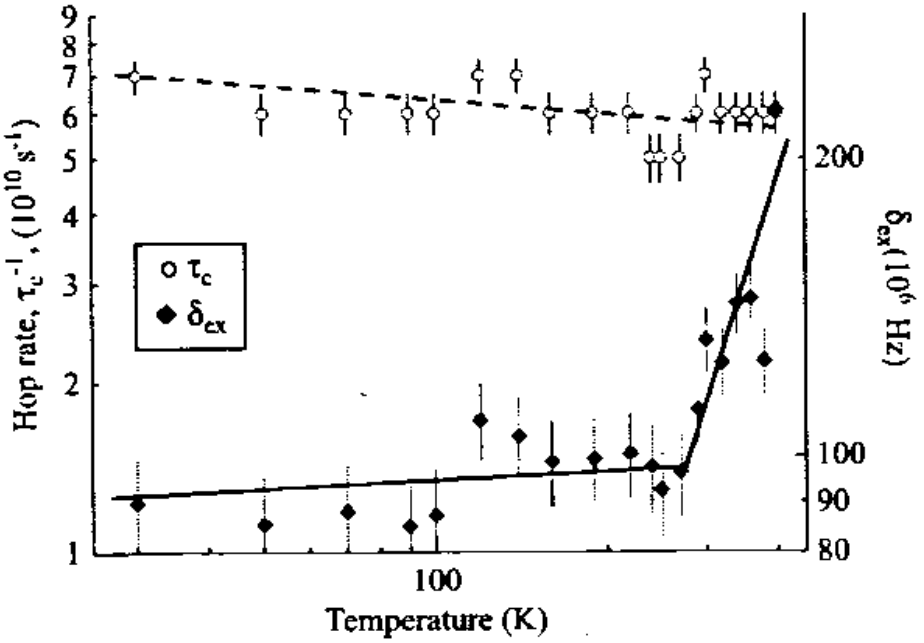

Figure 4.10: Hop rates, τ_c^{-1}, and nuclear hyperfine interaction, δ_{ex} of Mu_T in ^{13}C diamond as a function of temperature. Dotted and solid lines to guide the eye.

6×10^{10} s^{-1}; however, it may have a decreasing trend with increase in temperature. This value is larger than 10^{10} s^{-1} in the range of 10-400 K; a conformation of our preliminary conclusion based on Figures 4.7 and 4.8. Assuming that the Mu_T diffuses via the neighboring tetrahedral interstitial sites, the diffusion constant is deduced by $D = a^2\tau_c^{-1}/32$ where a=3.57Å for diamond is the lattice constant [41]. It then

follows that the diffusion constant is estimated to be $D_{\mathrm{Mu_T}} \approx 2.4 \times 10^{-6}$ cm^2/s. On the other hand, theoretical calculations show that the tunneling diffusion constant of hydrogen is estimated to be $D_{\mathrm{H}} \sim 10^{-12}$ cm^2/s [55]. The difference between $D_{\mathrm{Mu_T}}$ and D_{H} could be attributed to the difference in mass of the two species. This causes the zero point energy of $\mathrm{Mu_T}$ to be higher, and therefore, the barrier height will be lower (for further quantitative demonstration see, for example, [58]). The tunneling coefficient depends both on the barrier parameters and the mass of the particle. Hence, tunneling amplitude for $\mathrm{Mu_T}$ is larger and will be significant at much higher temperatures. Another aspect is the different time windows. $\mathrm{Mu_T}$ is observed after a few microseconds, while H has usually been measured after longer residence times, giving more opportunity for competing process to occur. At present, diamond is not sufficiently pure, and the many traps represented by defects disturb the diffusion measurements.

We note that the essentially constant τ_{c}^{-1} is inconsistent with classical diffusion. We further note that the temperature dependence of T_1^{-1} is due mostly to the temperature dependence of the nuclear hyperfine parameter: δ_{ex} varies slowly at round 90 MHz at lower temperatures, consistent with a previously measured value using TF-μSR measurements [56] but begins to increase rapidly between room temperature and 400 K. If muonium is indeed moving in a wavelike state below about 300 K, this parameter will be reduced according to the spread of the wave-packet: δ_{ex} is essentially the amount by which the local field varies as the muonium encounters spin-up and spin-down nuclei and so is reduced by an approximate factor $\sqrt{n}$ for delocalization over n sites. This argument was invoked to explain a similar variation of this parameter for muonium diffusion in NaCl [42] and appears equally appropri-

ate here. The increase in δ_{ex} above 300 K would in this model represent localization of the muonium wave-packet onto fewer sites as the tunneling changes character from coherent to incoherent: one can say that the scattering length is becoming comparable with the distance between adjacent sites or, in other words, that it is appropriate to change from a wavelike to a particle-like description.

Also, the temperature region for the increase in δ_{ex} corresponds to the onset of the thermally activated transitions of Mu_T to Mu_{BC}, i.e., from cage-centre to bond-centre [57]. This is entirely consistent with the requirement that the muonium wave function first becomes localized before the transition can occur. Reffering to Figure 4.3, however, it does appear that this conversion precludes observation of the anticipated mobility minimum for diffusion via neighboring T-sites as well as the eventual switch from phonon assisted tunneling to classical over-the-barrier diffusion [33,38,40,41]. We had expected to observe the power law dependence of the two-phonon quantum diffusion regime from about 150 to 400 K, based on the interpretations of previous TF-μSR measurements [31,38], so there is some ambiguity here that requires resolution in further experiments. The present work suggests that the power law dependence observed in T_1^{-1} reflects a variation of δ_{ex} and not τ_c^{-1}. Consequently, it appears that τ_c^{-1} is more consistent with Bloch state regime of the diffusion constant.

Chapter 5

Conclusion

Both TF- and LF-μSR results complement each other, namely indicating that the Mu_T state diffuses very fast at lower temperatures (below 200 K) in diamond. This fast diffusion appears to be in the band-like (Bloch) state, i.e undergoing coherent tunneling. In this case such diffusion is reflected through the interaction of the Mu_T state with the ^{13}C atoms. Not surprisingly, we seem to be observing fast quantum motion of Mu_T to relatively high temperatures in diamond, when considering the large Debye temperature ($\Theta_D \approx 2200$ K) of diamond and its rigid lattice that is known to have relatively shallower tetrahedral interstitial sites (~ 0.5 eV) [48]. The latter could enable the persistence of fast diffusion to relatively high temperatures [43], as evident in our results. The spin relaxation rate in the LF-μSR, T_1^{-1}, was attributed to the mobile Mu_T state found to be the only relaxing species in TF-μSR experiment.

In the LF-μSR experiment, the results show a very fast diffusion for interstitial muonium, Mu_T, diamond, consistent with a wavelike or Bloch-state regime. The power law behavior in the longitudinal spin relaxation observed here appears to be due to a temperature-dependent averaging of the nuclear hyperfine interaction. It remains to be shown that this is fully consistent with interpretation of the transverse spin relaxation, but the present results show the hop rate to be essentially constant in this temperature range, corresponding to diffusion constant that is several orders of magnitude larger than that of hydrogen. This difference could be attributed to different tunneling behaviors (due to different masses) of Mu_T and H as well as differing time windows within which Mu_T and H are studied in diamond. The thermal conversion of the mobile cage-centred species, Mu_T, to the immobile and more stable bond-centred state, Mu_{BC}, precludes exploration of the quantum diffusion above about 400 K.

Bibliography

[1] For a comprehensive review: J.E. Field, ed. The properties of natural and synthetic diamond (Academic Press, New York, 1992)

[2] Spear and Dismukes, Willey, Synthetic Diamond - Emerging CVD Science and Technology, New York (1994)

[3] K. Saarinen, C. Corbel, P. Hautojärvi, P. Lanki, F. Pierre., D. Vignaud, *J. Phys. Cond. Mat.* **2**(1990)2453

[4] M. Manninen, R.M. Nieminen, *Appl. Phys.* **A26**(1981)93

[5] K. Saarinen, P. Hautojärvi, A. Vehanen, R. Krause, G. Dlubek, *Phys. Rev.* **B 39**(1989)5287

[6] Sokrates T. Pantelides, *Appl. Phys. Lett.* **50**(1987)995

[7] M.I. Landstrass, K.V Ravi, *Appl.Phys. Lett.* **56**(1990)1454

[8] A.G. Ulyashin, R.B. Gelfand, N.V. Shiopak, A.M. Zaitiv, A.V. Deniseko, A.A. Melnikov, *Diamond Relat. Mater.* **2**(1993)1516

[9] D.G. Goodwin and J.E. Butler, in: Handbook of industrial diamonds and diamond films, eds. M.A. Prelas, G. Popovici and K. Bigelow (Marcel Dekker, New York, 1996), in press

[10] J.E. Buttler, R.L. Woodin, Phil.Trans. R.Soc.Lond. **A 342**(1993)1516

[11] K. Macnamara Rutledge, K.K Gleason, *Chem. Vap. Depos.* **2** (1996)37

[12] T.E. Beerling, C.R. Helms, *Applied. Phys. Lett.* **65**(1994)1912

[13] R.F. Davis, *Phys. Rev.*, **B 185**(1993)1-15

[14] W.J.P. van Enckevort, In Synthetic Diamond: Emerging Science and technology; K.E. Spear, J.P. Dismukes, Eds., John Willey and Sons: New York, 1994; pp. 307-54

[15] J.R. Dennison, M.W. Holtz, G.M. Swain, Spectroscopy (1996)10,38

[16] J.P.F. Sellschop, in: J.E. Field (ed), The properties of natural and Synthetic Diamond, Academic Press (1992) 81

[17] J.P. Goss, R. Jones, M.I. Heggie, C.P. Ewels, P.R. Briddon, S. Oberg, *Phys. Rev.* **B 65**(2002)115207

[18] D.D. Koleske, S.M. Gates, B.D. Thoms, J.N. Russell, Jr., and J.E. Butler, *J. Chem. Phys.* **102(2)**(1995)992

[19] B.D Thoms and J.E. Butler, *Surface Science*, **328**(1995)291

[20] S.P. Mehandru, A.B. Anderson and J.C. Angus, *J. Mater. Res.* **7**(1992)689

[21] T.L. Estle, S.K. Estreicher and D.S. Marynick, *Phys. Rev.* Lett. **58**(1987)1547

[22] P. Briddon, R. Jones and G.M. Lister, *J. Phys.* **C 21**(1988)L1027

[23] J. Goss, R. Jones, P.R. Briddon and S. Oberg. Proceedings of the diamond conference, Bristol, England (1997)

[24] I.Z. Machi, S.H. Connell, M. Baker, J.P.F. Sellschop, K. Bharuth-Ram, *Hyperfine Interactions* **136/137**(2001)727-730

[25] I.Z. Machi, MSc thesis 1996 (University of Durban-Westville, Durban- South Africa), (unpublished)

[26] G. Davies, S.C. Lawson, A.T. Collins, A Mainwood, S.J. Sharp, *Phys.Rev.* **B 46**(1992)13157

[27] E.B. Karlsson, in: Solid State Phenomena as seen by Muons, protons and Excited Nuclei (Oxford Science, 1995) p.31

[28] D.G. Eshchenko, V.G. Storchak, J.H. Brewer, G.D. Morris, M.A. Clarker-Gayther, S.P. Cotrell, S.F. Cox and J.S. Lord, *Physica B: Condensed Matter* **289-290**(2000)421-424

[29] F.P. Bundy, The P,T phase and Reaction diagram for elemental Carbon, 1979; *J. Geophys. Res.* **85 (B 12)**(1980)6930

[30] I.Z. Machi, Hydrogen-impurity/Defect Complexes in Diamond: PhD thesis, 2000

[31] I.Z. Machi, S.H. Connell, J.P.F. Selleschop, K. Bharuth-Ram, B.P. Doyle, R.D. Maclear, J. Mayor, and R. Scheuermann, Physica**B 289-290**(2000)468

[32] G.D. Morris, PhD thesis (University of British Columbia, Canada) (1998), unpublished

[33] V.G. Storchack, N.V. Prokof'ev, *Rev. Mod. Phys.* **70**(1998)929

[34] B.D. Patterson, *Rev. Mod. Phys.* **60(1)**(1988)66-158

[35] V. Storchack, J.H. Brewer, G.D. Morris, *Hyp. Int.* **97-98**(1996)323

[36] S.J. Blundell, *Contemporary Physics*, **40**(1999)175

[37] J.E. Field, The properties of diamond (Academic Press London, 1992)

[38] I.Z. Machi, S.H. Connell, M. Dalton, M.J. Sithole, K. Bharuth-Ram, S.F.J. Cox et al, *Diam. and Relat. Mater* **13**(2004)909-913

[39] S.F.J. Cox, *Solid State Nucl. Magn. Reson.* **11**(1998)103

[40] R.F. Kiefl, R. Kadono, J.H. Brewer, G.M. Luke, H.K. Yen, M. Celio et al, *Phys. Rev.* **B43** (1989)792

[41] R. Kadono, R.F. Kiefl, J.H. Brewer, G.M. Luke, T. Pfiz, T.M. Riseman et al, *Hyp. Int.* **64**(1990)635.

[42] R. Kadono, *Hyp. Int.* **64**(1990)615

[43] A.M. Stoneham: In the properties of Natural and Synthetic diamond, by J.E. Field Academic Press, London 1992, pp 1-34

[44] S.P. Mehandru, A.B. Anderson, *J. Mater. Res.* **9**(1994)383

[45] S.H. Connell, J.P.F Selleschop. J.E. Butler, R.D. MacLear, B. Doyle and I. Machi, *Diamond and Related Materials* **7**(1998)1714-1718

[46] E. Holzchuh, W. K*ü*ndig, P.F. Meier, B.D. Patterson, J.P.F. Sellschop, M.C. Stemmet, and H. *Appel, Phys. Rev.* **A25** (1982)1272

[47] S. Kalbitzer: in Fundamental and applied Aspects of Modern Physics, by S.H. Connell and R. Tegen, World Scientific Publishing co, 2001, pages 422-432

[48] J.P. Goss, *J. Phys. :Condens. Matter* **15** (2003)R551-R580

[49] R. F. Kiefl, W. Odermatt, Hp. Baumeler, J. Felber, H. Keller, W. Kndig, P. F. Meier, B. D. Patterson, and J. W. Schneider, *Phys. Rev.* **B 34** (1986)1474-1484

[50] J. Goss, P.R Briddon, R. Jones, *Phys. Rev.* **B69** (2004)no-165215

[51] M. Harting, D.F. Kanguwe, C.M. Comrie, S. Nsengiyumva, S.R. Naidoo, T.E. Derry and D.T. Britton, *Material Science Forum* **Vols. 445-446** (2004)pp 102-104

[52] I.Z. Machi S.H. Connell, J.P.F Selleschop, and K. Bharuth-Ram, *Hyperfine Interactions* **136/137** (2001)727-730

[53] J.M. Baker, I.Z. Machi, S.H. Connell, K. Bharuth-Ram, J.E. Butler, S.F.J. Cox, C.G. Fischer, T. Jestadt, R.W.N. Nilen and J.P.F. Selleschop, *Hyperfine Interactions* **120/121** (1999)579-583

[54] V. Storchak, S.F.J Cox, S.P. Cottrell, J.H. Brewer, G.D. Morris and N.V. Prokof'ev, Phys. Rev. **B53** (1996)662-667

[55] S. Kalbitzer, in: S.H. Connell, R. Tegen (Eds.), Fundamental and applied Aspects of Modern Physics, World Scientific Publishing, 2001, p. 422

[56] J.W. Schneider, R.F. Kiefl, K.H. Chow, S. Johnston, J. Sonier, T.L. Estle, et al., *Phys. Rev. Lett.* **71(4)** (1993)557

[57] D. Gxawu, I.Z. Machi, S.H. Connell, K. Bharuth-Ram, M.J. Sithole, S.F.J. Cox, *Diam. and Relat. Mater* **14** (2005)375-379

[58] H.J. Pain, The Physics of Vibrations and Waves, (John Willey, Chichester, 2005)267-304